Journal of The Electrochemical Society, 2024 **171** 024505

Catalyst-Specific Accelerated Stress Tests in Proton Exchange Membrane Low-Temperature Electrolysis for Intermittent Operation

Shaun M. Alia,[1,*,z] Kimberly S. Reeves,[2] Haoran Yu,[2] Jae Hyung Park,[3] Nancy N. Kariuki,[3] A. Jeremy Kropf,[3] Deborah J. Myers,[3,] and David A. Cullen[2,*]**

[1]*Chemical and Material Sciences Center, National Renewable Energy Laboratory, Golden, Colorado, United States of America*
[2]*Center for Nanophase Materials Sciences, Oak Ridge National Laboratory, Oak Ridge, Tennessee, United States of America*
[3]*Chemical Sciences and Engineering Division, Argonne National Laboratory, Lemont, Illinois, United States of America*

Device-level stress tests are developed that focus on anode catalyst layer degradation and future anticipated operating conditions, including intermittent load and reduced platinum group metal content. Square-wave cycles with an upper load limit of 2.5 A cm^{-2} are utilized to screen commercial iridium (Ir) materials. Performance losses are primarily due to decreasing kinetics and are accompanied by catalyst migration into the membrane, worsening catalyst/ionomer integration, and weakening of the catalyst/membrane interface. For ruthenium-containing catalysts, the in situ performances are higher but durabilities lower than Ir baselines, and any performance advantage is lost within the test. Increased loss is likely due to the higher dissolution rate; microscopy confirmed greater degrees of ruthenium migration. For Ir metal or mixed oxides, ex situ activity improvements generally did not translate to in situ performance. The durability, however, is significantly lower and the loss rate increased from 3 (oxide) to 9 (metal) μV $cycle^{-1}$. These results are consistent with historical findings in literature, rationalize the continued use of iridium oxide as a baseline catalyst, and demonstrate that traditional catalyst development approaches may not improve device-level durability when focused on low-cost applications. A shift in focus may therefore be more effective at improving catalyst utilization and lessening load requirements.

 [DOI: 10.1149/1945-7111/ad2735]

Manuscript submitted December 1, 2023; revised manuscript received January 31, 2024. Published February 23, 2024.

Hydrogen and electrochemical water splitting in particular have been limited in commercial use due to the production cost. Recent cost reductions to renewable power sources, however, allow for decreases in electrolysis feedstock costs, and further capital cost reductions can enable significant hydrogen and electrolysis growth.[1–4] As renewable grid contributions increase, hydrogen is uniquely positioned for long-term storage in grid support.[5] Additionally, hydrogen can be offloaded to other industries and growth opportunities are anticipated in transportation, chemicals, and agriculture.[2]

In addition to the feedstock, capital cost reductions are critical to improving the commercial viability and use of electrolysis. A majority of system cost reductions are expected through manufacturing, including larger stack size, increased production rates, and economies of scale.[1] To some extent in proton exchange membrane (PEM) -based electrolysis, however, platinum (Pt) group metal (PGM) loading reductions in the catalyst layers and other component coatings (transport layers, separators) will be used to minimize the cost of traditionally overengineered systems.[1,3]

In this regard, cost and durability are interlinked and involve tradeoffs, and significant increases to performance loss rates have been found when accounting for intermittent power inputs and lower PGM loading.[6–9] Numerous component studies have evaluated the degradation of catalyst layers,[6,10–24] transport layers,[14,25–32] and the membrane,[17,33,34] and have identified relevant loss mechanisms. While several component and degradation processes need to be incorporated for device-level accelerated stress tests, anode catalyst performance loss is of particular interest because these losses and the resulting device lifetime affect materials (loading) and operational (cycling frequency, load input) requirements.[6,35] Past efforts have evaluated catalyst layer degradation during intermittent and start-stop operation, finding that performance losses occur through catalyst dissolution/migration, catalyst layer changes (agglomeration, porosity), and interfacial weakening or tearing.[6,18,24]

In this study, accelerated stress tests have been explored for the anode catalyst layer that focus on intermittent operation. To isolate this loss mechanism, operational choices were made to minimize oxidation changes of the anode catalyst, membrane degradation (no applied/cycled backpressure), and transport layer degradation (commercial transport layers). Low catalyst loadings and high cycling frequency were utilized to accelerate performance losses and were previously found to be representative of less aggressive operation (higher loading, constant input) in terms of how losses appear during in situ testing and how they correspond to catalyst layer changes.[18] These stress tests screen several iridium (Ir) -based commercial materials as anode catalysts, and focus on typical catalyst improvements including ruthenium (Ru) inclusion and the use of materials with different degrees of ex situ oxidation. While past efforts focused on applied cell potential to evaluate loss mechanisms, galvanostatic procedures may be more relevant to anticipated operation and reflect materials improvements that can potentially lessen load requirements and durability losses.[18] Studies evaluating stress tests and electrolysis degradation are critical to developing lifetime models, improving our understanding of cost/durability through technoeconomic analysis, and developing mitigation strategies to limit loss.

Experimental

Membrane electrode assemblies (MEAs) were prepared as catalyst coated membranes with loadings of 0.1 mg cm^{-2} (anode/cathode, metal basis). For catalyst screenings, MEAs used Nafion 117. Nafion 115 and 212 were also evaluated to separate the impact of current density from cell potential. Catalyst layers were coated with an Accumist ultrasonic spray head in an automated spray station. Cathodes were prepared first with carbon-supported Pt (Pt/HSC, 47 wt% Pt) from Tanaka Kikinzoku Kogyo (TEC10E50E) using previously developed methods.[24] To spray four cathodes, 91.9 mg of Pt/HSC was added to 24 ml water and 18.3 ml n-propyl alcohol. The ink was cooled in ice for 5 min, then 109.9 μl of

*Electrochemical Society Member.
**Electrochemical Society Fellow.
[z]E-mail: shaun.alia@nrel.gov

ionomer (DE2020, 20 wt%) was added to the ink prior to sonication (30 s horn, 20 min bath, 30 s horn). Following sonication, the ink was immediately added to a syringe pump and sprayed at 0.2 ml min^{-1} onto the membrane held to a vacuum plate at 80 °C.

Ir-based anodes were prepared using previously developed methods. The materials screened as oxygen evolution (OER) catalysts included Alfa Aesar unsupported Ir oxide (43396), Tanaka Kikinzoku Kogyo unsupported Ir (US171109), Johnson Matthey unsupported Ir (C2025/160000), Umicore unsupported Ir (0363/00-I4), Premetek unsupported Ir (P40V010), Furuya unsupported IrRu (1267905), Alfa Aesar unsupported Ru (11804), Umicore titania-supported Ir oxide (73.35 wt% Ir, 0821/01-D5), and Premetek carbon-supported Ir (20 wt% Ir, P40A200).[24] To spray four anodes, 113.8 mg of catalyst (Ir/Ru metal basis) was added to 11.7 ml water and 23.8 ml n-propyl alcohol. The ink was cooled in ice for 5 min, then 95.6 μl of ionomer (DE2020, 20 wt%) was added to the ink prior to sonication (30 s horn, 20 min bath, 30 s horn). Following sonication, the ink was immediately added to a syringe pump and sprayed at 0.2 ml min^{-1} onto the membrane held to a vacuum plate at 90 °C.

Different ink properties and spray parameters were required for optimum anode/cathode catalyst layer uniformity and performance. For unsupported iridium catalysts, inks tended to be less stable and were likely impacted by the less heterogeneous primary particle and aggregate/agglomerate sizes.[36] The electrode fabrication processes used in this study leveraged past work focused on the optimization of catalyst layers and cell performance by tuning ink composition and spray parameters, including ink solid concentration, ink water/alcohol and ionomer content, spray rate, and spray temperature.[24] A higher spray temperature specifically was required to increase the drying rate of sprayed ink, and to prevent catalyst layer nonuniformity.

After spraying the catalyst layers, the catalyst coated membranes were rehydrated in water for at least 5 min, then dried at 50 °C on a vacuum plate. This process slightly thinned the membrane, but was needed to minimize warping from the spray process, to improve cell performance, minimize contact resistance, and prevent leaking. Following this processing step, catalyst loadings were evaluated by X-ray fluorescence (XRF) with a Fischer XDV-SDD energy dispersive spectrometer. Loadings were averaged over four 30 s measurements.

MEA testing was completed as 25 cm^2 single-cells, using aluminum endplates (Fuel Cell Technologies), Pt-coated titanium PTLs and flow fields (anode, Giner Inc.), and carbon transport layers and flow fields (cathode, Fuel Cell Technologies). Tests were completed on Greenlight stands with an anode water flow rate of 0.3 L min^{-1} (dry cathode, no backpressure) and at 80 °C. Cells were conditioned with holds at 0.2 A cm^{-2} for 1 h, 1 A cm^{-2} for 1 h, and 1.7 V until the current stabilized (<0.5 mA change over 1 h). These protocols leverage past efforts benchmarking PEM electrolysis performance across various laboratories.[37] While current or voltage holds can be used to condition MEAs, these procedures mixed approaches, and were intended to gradually condition MEAs and promote consistent performance determinations. Anodic polarization curves were then taken followed by cathodic polarization curves. Each step was held for 5 min and the reported cell potential was the average over the last min. Other components (polymer, PTL), ink formulations, and catalyst layer properties can have significant effects on catalyst utilization, performance, and durability in MEA testing.[24,38] For PTLs specifically, substructure and coating properties can influence polarization curves through ohmic (contact resistance, sub coating passivation), kinetic (utilization), catalyst layer resistance (utilization and proton/electron pathways), and residual (bubble transport) losses, as well as how these losses change over time.[38]

Diagnostics were then taken and included cyclic voltammograms in the potential range 0.025–1.3 V at 50 mV s^{-1} and impedance spectra in the frequency range 1 Hz–100 kHz for each data point taken during polarization curves. The high frequency resistance values from impedance spectra were used to correct polarization curves for kinetic comparisons. Kinetics were evaluated through Tafel plots of HFR-corrected potentials and used to determine exchange current densities. Ohmic, kinetic, and transport overpotentials were also tracked and presented. Ohmic overpotentials were calculated based on the difference between the cell potential corrected and uncorrected for HFR. Kinetic overpotentials were calculated based on the difference between kinetics (Tafel plot) and the thermodynamic potential, with corrections for entropy and partial pressure (624 mm Hg at 5674 ft). Transport overpotentials were calculated based on the difference between the cell and thermodynamic potentials unaccounted for by ohmic/kinetic loss.

To evaluate multiple options for accelerated stress tests, several membrane thicknesses and upper current limits were tested. For catalyst screening, 31,500 60 s cycles were used, with 30 s at 2.5 A cm^{-2} followed by 30 s at 0 A cm^{-2} at 80 °C. The upper current limit was chosen to optimize the performance loss rate at this anode catalyst layer loading (0.1 mg cm^{-2}) and experiment duration (525 h). The repeated, frequent cycling was used to accelerate losses and minimize experiment duration, and was previously found to be representative of renewable load profiles in how losses appeared during in situ testing and how they corresponded to catalyst layer changes.[18] Throughout durability testing (31,500 cycles), polarization curves and diagnostics were taken every 4,500 cycles, with the cycle counts chosen for feasibility and to ensure that the test duration was longer than 500 h (525). Stress tests in this case were based on current since galvanostatic testing may be more relevant to anticipated operation and reflects materials improvements that can potentially lessen load requirements and durability losses.[9] Additionally, a protective lower potential limit was set to 1.4 V to ensure that the catalyst layer did not go through redox cycling due to hydrogen crossover during the down cycle (0 A cm^{-2}).[6,20] Past efforts have evaluated the impact of hydrogen crossover and catalyst layer redox on durability testing, finding significantly higher performance losses.[6,20] The intent of this study was to focus on intermittent operation without the complications of redox and assumes that materials (recombination catalyst) or operational (short-term storage) mitigation strategies will minimize the occurrence and impact of catalyst redox transitions.

Performance and durability testing that varied the membrane thickness, applied current cycle, and anode catalyst was completed on 3 MEAs to evaluate reproducibility and statistics. Figures of polarization curves (performance) and loss rates (durability) included error bars of standard deviation to reflect these statistics; figures of polarization curves during stress tests and post-test characterization were of MEAs closest to the average. In general, the error bars were relatively small and likely due to the MEA iterations having been sprayed at the same time and with the same ink batch, with differences in performance/durability beyond statistical error. Greater variance, however, is expected spray-to-spray and ink/spray optimization can significantly affect cell performance and durability.[24]

These stress tests are not intended as field tests and focus on anode catalyst layer degradation, low catalyst loading, and frequent cycling to accelerate loss observations. Additional components (membrane, transport layers) and catalyst layer degradation processes (contaminants, manufacturing defects) need to be incorporated to develop device-level accelerated stress tests and lifetime models, and to better inform technoeconomic analysis. Square-wave testing was intended to aggressively accelerate loss rates and was previously compared to wind and solar profiles to ensure consistency in how in situ performance losses were observed.[18] Over a ten year period, solar profiles can expect to cycle once per day (3650 times), although the upper stressor will vary based on input and stack sizing. Wind profiles can induce more variability and cycle high/low input more or less frequently. Past efforts used wind profiles with twice per day turn downs (7300 times over ten years), that may overestimate the cycling frequency in other locations.[18]

Rotating disk electrode testing was completed with an Autolab PGSTAT 302 N potentiostat using polycrystalline gold working electrodes, gold counter electrodes, and a reversible hydrogen reference electrode (RHE). Working electrodes were prepared by previously published methods and inks contained 3.5 mg catalyst (Ir/Ru metal basis), 7.6 ml water, and 2.4 ml isopropanol to produce electrodes with a catalyst loading of 17.9 $\mu g\,cm^{-2}$ (metal basis).[39] After the ink was iced for 5 min, 20 μl of Nafion ionomer (Sigma Aldrich, 5wt%) was added and the ink was sonicated to disperse the catalyst (30 s horn, 20 min bath, 30 s horn). Following sonication, 10 μl of ink was pipetted onto a polycrystalline gold electrode that was inverted on a rotator (Pine Research Instrumentation, MSR type) at 100 rpm. After pipetting the ink, the rotation was increased to 700 rpm and the electrode allowed to dry for 20 min (room temperature).

Electrochemical characterization of catalysts started with conditioning, 50 cycles in the potential range 1.2–1.8 V vs RHE at 2500 rpm and 100 mV s^{-1} in a nitrogen saturated 0.1 M perchloric acid electrolyte at room temperature. Linear sweep voltammograms were then completed at 20 mV s^{-1}, the first iteration in the potential range 1.2–1.6 V vs RHE to focus on kinetics and the second iteration in the potential range 1.2–2 V vs RHE to capture the entire region of interest. Both evaluations were completed with a built-in current interrupter to correct for internal resistance (25 ± 1 Ω), to avoid inaccuracies with corrections after data acquisition. Electrochemical surface areas (ECAs) were determined by hydrogen underpotential deposition and mercury underpotential deposition, by previously published methods.[40,41] For hydrogen underpotential deposition, cyclic voltammograms were completed in the potential range 0.025–1.5 V vs RHE at 20 mV s^{-1} in a nitrogen-saturated 0.1 M perchloric acid electrolyte. ECA measurements from hydrogen underpotential deposition were used to quantify Ir/Ru metal sites available on catalyst surfaces. ECA values were calculated from the charge conversion of an adsorbed monolayer on Ir (179 $\mu C\,cm_{Ir}^{-2}$) and Ru (125 $\mu C\,cm_{Ru}^{-2}$), and were based on previous measurements taken with polycrystalline Ir and Ru electrodes.[40] Approximations for mixed materials (Furuya IrRu) were based on bulk composition by inductively coupled plasma mass spectrometry (ICP-MS). For mercury underpotential deposition, voltammograms were completed in the potential range 0.025–0.55 V vs RHE at 20 mV s^{-1} in a nitrogen-saturated 0.1 M perchloric acid electrolyte containing 1 mM mercury nitrate. ECA values were calculated from the charge conversion of an adsorbed monolayer on Ir (358 $\mu C\,cm_{Ir}^{-2}$) and Ru (301 $\mu C\,cm_{Ru}^{-2}$), and were based on previous measurements taken with polycrystalline Ir and Ru electrodes.[40] For ECA measurements, the Coulombic charge correction varies based on the element and the facet distribution evaluated. For Ir/Ru comparisons, the Ru Coulombic charge was lower for the adsorption of both a proton and mercury monolayer. These ECA determinations are related to site-access and not explicitly a measure of OER reactivity, and the data presented was consistent with historical findings in that Ru-containing catalysts were more active for OER than Ir-only materials.[42] Approximations for mixed materials (Furuya IrRu) were based on bulk composition by ICP-MS. Additionally, capacitances were evaluated from cyclic voltammograms in the potential range 0.8–1.4 V vs RHE. Psuedocapacitances at a lower potential range were not calculated due to the proximity of current responses from hydrogen underpotential deposition and redox transitions, and how significant changes to porous transport layer (PTL) site-access and catalyst near-surface metal/oxide content could change these values. Capacitances at higher potential may not be reflective of site-access, and past studies have noted significant differences between kinetic performance and the current responses in cyclic voltammograms.[43] These values were used qualitatively, however, to compare differences in oxide content between catalysts and catalyst layer changes (subsurface oxide growth, electrode thinning) in extended operation.

Following initial testing, catalysts were evaluated for durability with potential holds for 13.5 h at room temperature.[39,44] Electrolyte aliquots (5 ml) were taken at 0.5, 1, 4, and 13.5 h and quantified with ICP-MS to determine dissolution rates. ICP-MS was taken with a Thermo Scientific iCAP Q in kinetic energy discrimination (KED) mode. The ICP-MS was calibrated to internal standards, a blank, and Ir/Ru standards at 2, 20, and 200 ppb which resulted in instrument detection limits (IDL) of less than 2 ppt.

In ex situ measurements, bubble formation lowers site-access and impacts performance and durability assessments.[39,44] Catalyst activities, before and after durability testing, were made during voltammograms to avoid the transport issues associated with chronoamperometry experiments.[39] To minimize the impact of gas blinding on activity evaluations, electrodes are also rinsed/dried following condition and potential holds (prior to any activity measurement), to normalize the activity of each electrode to one another (reproducibility) and to their initial performance (for durability). To minimize the impact on durability results, activity evaluations were made during voltammograms after the stress tests and the raw current was not reported, since bubble formation limits site-access and can lower activity in a way that is not representative of a relevant loss mechanism.[39] For Ir oxide (Alfa Aesar, 43396), minimal activity loss and dissolution were found following a 2 V hold, indicating that bubble formation did not create artificial loss. Higher ECA losses for other catalysts (by mercury underpotential deposition) also corresponded to increased dissolution, indicating that transport or gas blinding did not increase loss rates. Transport, however, affects durability and dissolution measurements, and bubble formation can lessen these losses by preventing full site-access for the stress test duration. While OER transport losses are larger in rotating disk electrodes than MEAs, gas blinding may occur in MEAs as well and past efforts have seen lower loss rates than expected during stress tests at higher potential/current density.[18]

In rotating disk electrode testing, gold substrates were used due to its conductivity, durability at low pH and experiment potentials relative to other readily available options, and low participation in OER. Working electrode substrates may dissolve in small quantities that can lead to catalyst layer delamination, underestimating catalyst dissolution rates, and overrepresenting activity loss rates. Gold dissolution was not seen as a significant contributor to activity/dissolution measurements since minimal amounts of gold were found in ICP-MS, and past efforts evaluating Ir metal and Ir oxide durability found reasonable agreement between activity loss and dissolution rate.[39] Past studies further compare gold substrates to less stable materials (carbon), to demonstrate how this gap in activity loss and dissolution can be impacted by substrate instability.[39] The rotating disk electrode test protocols used leverage past baselining and benchmarking efforts in acidic OER.[39,45]

X-ray diffraction (XRD) patterns were taken with a Bruker D8 Discover, operated at 40 kV and 35 mA in the 2θ range 13.5–88° for 2 h. Powders were attached by carbon tape to a silica slide. Calculations of catalyst crystallite size were made through Rietveld refinement with Match 3.2.2 and FullProf 2.05.

The catalyst particle size distributions (PSDs) were determined using small-angle X-ray scattering (SAXS). The anode catalyst layer samples were prepared for the SAXS measurements by transferring the layers from the membrane to single-sided, transparent Scotch™ tape, which has a low X-ray scattering background. The SAXS data were acquired at beamline 9-ID-C at the Advanced Photon Source (APS), Argonne National Laboratory equipped with a combined Bonse–Hart (ultra-small X-ray scattering, USAXS) and pinhole (small angle X-ray scattering, SAXS) instrument. The incoming X-ray beam was monochromatized, via a pair of Si (220) crystals, to an energy of 21 keV. The optics and instrumentation details for this scattering beam line have been previously reported.[46] The size of the X-ray beam for the USAXS measurements was 0.8 × 0.6 mm (horizontal x vertical) and 0.8 × 0.2 mm for the SAXS measurements. The exposure times for each sample were 90 s for USAXS and 30 s for SAXS. During data reduction, patterns collected on a blank piece of Scotch™ tape were subtracted from the patterns acquired for the samples. The data were corrected and reduced with

the NIKA software package,[47] and data analysis was conducted using the IRENA software package[48] running on the IGOR Pro 7.0 (Wavemetrics) platform.

Catalyst PSDs were obtained from the measured scattering data using the maximum entropy (MaxEnt) method,[49] involving a constrained optimization of parameters to solve the scattering equation:

$$I(q) = |\Delta\varrho|^2 \int |F(q, r)|^2 \, (V(r))^2 Np(r) dr$$

Where, I(q) is the scattered intensity, ϱ is the scattering length density of the particle, F(q, r) is the scattering function at scattering vector q of a particle of characteristic dimension r, V is the volume of the particle, and N_p is the number density of particles in the scattering volume.

Iridium L_2-edge extended X-ray absorption fine structure (EXAFS) data were acquired for the entire catalyst-coated membranes (CCMs) at APS beamlines 10-BM and 10-ID of the Materials Research Collaborative Access Team. The L_2 edge was chosen rather than the L_3 edge to avoid interference in the extended region of the spectra from Pt fluorescence arising from the cathode catalyst layer. Data reduction and analysis were performed with the Athena software package.[50] The oxidation state of the Ir in the CCMs was evaluated by fitting the X-ray absorption near edge (XANES) regions of the spectra from −20 eV to 30 eV (vs an E_o of 12823 eV) to the spectra of two Ir-containing standards (Ir metal and IrO_2), representing the 0 and 4+ oxidation states, using the linear combination algorithm of the Athena software.

Results and Discussion

Initial screenings for durability protocols used unsupported Ir oxide (IrO_2) nanoparticles (Alfa Aesar, 43396). This catalyst was used as a baseline due to reasonable MEA performance and durability, and the relatively low dissolution rate compared to Ru and substoichiometric oxides. Past efforts further confirmed approximate oxide composition with electrochemical and materials characterization.[39,51]

Testing included varying the membrane thickness in the range 51–183 μm (Nafion N212, N115, N117) to evaluate the impact of membrane choice on catalyst layer durability. Membrane thickness has a clear effect on hydrogen crossover rates and can impact catalyst layer durability from redox during start-stop operation.[10,20] This evaluation focused on intermittent operation and avoided redox with a protective, lower potential limit during cycling (1.4 V). Testing with a lower potential limit ensures that the potential between the current collectors does not drop below 1.4 V. This limit, however, did not guarantee that all catalyst sites were exposed to the same potential, and isolated or insulated particles or small portions of the catalyst layer may have created variability in the exposed potential and degradation rate. Initially, higher performance was observed with thinner membranes and generally reflected the lower HFR values (33 mΩ cm^2 for N212, 121 mΩ cm^2) and ohmic loss (Figs. 1a, 1b). Some differences in kinetics were also found but were generally small, and exchange current densities varied between 0.0105–0.0113 mA cm^{-2} (8% difference). Stress tests were completed with 60 s cycles, 30 s at 2.5 A cm^{-2} followed by 30 s at 0 A cm^{-2} (1.4 V protective lower limit).

HFRs can be impacted by several factors, including polymer properties and thickness, interfacial contact resistances, and resistances through other components (catalyst layer, transport layer). Other components and interfaces equal, the HFR is driven by the polymer and in this instance where the polymer chemistries and properties were similar (N117, N115, N212), the change in HFR was primarily dictated by the membrane thickness. While there may be some slight variability in resistance due to differences in contact during fabrication (spraying, flattening) and testing (creep), the correlation between membrane thickness and resistance appeared reasonable.

With this protocol, the overall performance loss rates were similar, 3.3 μV $cycle^{-1}$ for N117, 2.8 μV $cycle^{-1}$ for N115, and 2.7 μV $cycle^{-1}$ for N212 (Figs. 1c–1e). From these results, membrane/ohmic losses appeared to be largely independent of performance changes and the loss rate may be more a function of the HFR-free potential than the total cell potential. If overpotential increases had been solely a function of cell potential, much smaller losses were expected with N212 (approximately 1 μV $cycle^{-1}$) when extrapolating loss rates at this loading, test profile (cycle type, frequency), and potential range.[18] Similarities in the performance loss rate can be due to multiple factors. First, the potential difference between the anode catalyst layer and membrane interface may drive catalyst dissolution/migration during in situ testing. The current density or the gas generation rate may also drive some catalyst layer changes (porosity, defect formation) and weakening or tearing at the catalyst layer/membrane interface. Although similar loss rates were observed, the rate slightly decreased with thinner membranes. Large, sudden fluctuations in load may create nonuniform potentials within the anode catalyst layer that can partially reduce portions (either to intermediate states or metal) and increase loss when operation resumes due to higher dissolution rates. Reducing the membrane thickness may slightly lessen these nonuniformities by reducing the increase/decrease in cell potential and slightly lower the performance loss rate.

In addition to assessing the impact of membrane thickness, upper current densities were evaluated and included 2, 2.5, and 3 A cm^{-2} (Fig. 2). In all cases, testing was completed with Nafion 117 to minimize crossover and with 60 s square-wave cycles, 30 s at the specified upper current density followed by 30 s at 0 A cm^{-2}. MEA performance losses increased with higher upper current densities, from 1.8 μV $cycle^{-1}$ (2 A cm^{-2}) to 4.5 μV $cycle^{-1}$ (3 A cm^{-2}) and the increase in loss rate was expected and likely due to the higher potential (catalyst dissolution, migration) and gas generation rates (interfacial tearing, catalyst layer structure changes). When evaluating diagnostics, several similarities were observed. Regardless of the upper current density limit, higher performance losses were generally due to kinetics, although slight increases in ohmic/transport loss were observed as well. Additionally, consistent features were found in impedance spectra (higher HFR, polarization resistance), cyclic voltammograms (thinning capacitance), and exchange current densities (large decrease), and varied only by degree. For catalyst screening with stress tests, an upper current density of 2.5 A cm^{-2} was used to produce a moderate loss rate. A lower operating current density was avoided to ensure that the loss rate was large enough to minimize MEA test statistics (reproducibility). A higher operating current density was also avoided to keep the cell potential below 2.5 V near the end of testing, particularly for catalysts that were less durable. In past efforts and isolated instances (simulated start-stop operation), extensive degradation of thin catalysts layers migrated small portions of the PTL coating into the catalyst layer, that may have accelerated kinetic losses (lower OER reactivity of platinum) and combined degradation mechanisms. Capping of the upper potential limit was done to avoid PTL degradation, to ensure that the loss mechanism remained consistent, and to avoid overrepresenting the loss rates of highly degraded catalysts.

Anode catalysts were screened with the stress test, which consisted of 60 s square-wave cycles (31,500 cycles), 30 s at 2.5 A cm^{-2} followed by 30 s at 0 A cm^{-2}. Several materials were evaluated, including Ir-/Ru-based and supported/unsupported nanomaterials. These experiments were used to assess whether differences in catalyst activity or stability can mitigate MEA performance losses in durability testing. This effort was not an endorsement of a specific catalyst or manufacturer, and testing included several catalysts that were not developed for PEM electrolysis use. Additionally, significant variability in catalyst properties (particle size, structure, oxide content) have been found for several material sets between batches and over time, and specific results are likely to change with both materials and integration enhancements. Current-based durability experiments further add complications since catalyst layer integration can have a

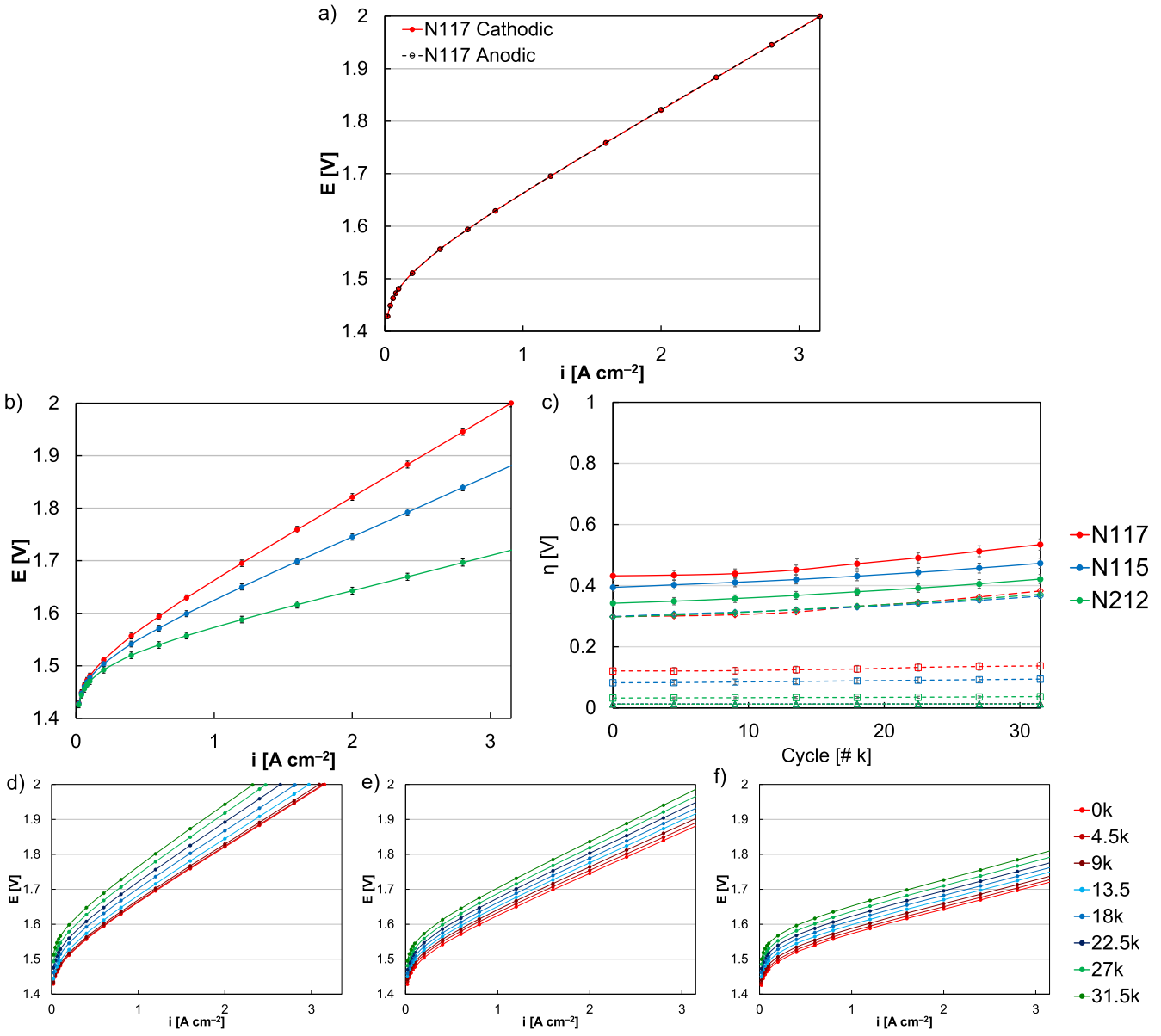

Figure 1. (a) Anodic and cathode polarization curve of MEA with N117. (b) Initial polarization curves of MEAs with N117 (red), N115 (blue), and N212 (green) at 80 °C. (c) Changes to overpotential in durability testing for MEAs with N117 (red), N115 (blue), and N212 (green). Losses were included for the total overpotential (solid line, filled circles) and due to kinetics (long dashed line, open diamonds), ohmic (short dashed line, open squares), and transport (dotted line, open triangles). Changes to polarization curves as a function of durability testing for MEAs with (d) N117, (e) N115, and (f) N212. Durability testing was completed by square-wave current density cycles, 30 s at 2.5 A cm^{-2} followed by 30 s at 0 A cm^{-2} at 80 °C.

significant effect on performance, and in turn an impact on durability.[24] Catalyst layers in this study were sprayed based on previous optimization efforts, and differences in materials integration (spray/ink parameters) for a larger materials set may similarly impact device-level performance and durability.[24]

Catalysts were compared based on changes in overpotential at 1 A cm^{-2} and were segregated into Ir-only and Ru-containing/supported materials (Fig. 3). For the Ir-only catalysts, initial performances were similar and within 43 mV at 1 A cm^{-2} (11 mV when excluding Umicore Ir, Fig. 3a). The large differences in durability, specifically for Johnson Matthey Ir (8.2 μV $cycle^{-1}$), Umicore Ir (8.5 μV $cycle^{-1}$), and Premetek Ir (8.9 μV $cycle^{-1}$), were therefore likely due to the high metal content increasing Ir dissolution.[39,51] Compared to the baseline Ir oxide (Alfa Aesar), the TKK Ir initially resulted in a slightly lower overpotential (10 mV at 1 A cm^{-2}). A higher loss rate (3.7 μV $cycle^{-1}$), however, was found that negated the performance advantage following durability testing and was also likely due to the mixed oxide content resulting in slightly higher degrees of dissolution.

For supported or Ru-containing catalysts, a larger range of durabilities were found (3.3–11 μV $cycle^{-1}$). Within the Ru materials, both Alfa Aesar Ru (23 mV) and Furuya IrRu (15 mV) initially showed lower overpotential than the Ir oxide baseline (Alfa Aesar). These advantages, however, were also lost in durability testing. After 31,500 cycles, the overpotentials were 7 mV (Furuya IrRu, 4.0 μV $cycle^{-1}$) and 45 mV (Alfa Aesar Ru, 5.4 μV $cycle^{-1}$) higher, and the higher loss rate was likely due to the increased dissolution rate of Ru. The Ru catalysts, however, were primarily oxides and the performance losses were less than Ir metal, consistent with past efforts evaluating ex situ dissolution.[52] Within supported catalysts, the Um Ir/Ti loss rate (4.9 μV $cycle^{-1}$) was also higher than the Ir oxide baseline in spite of the high oxide content. The increase in performance loss was likely affected by the initial lower performance (22 mV higher overpotential at 1 A cm^{-2}) which may have slightly increased catalyst dissolution/migration by exposing the anode

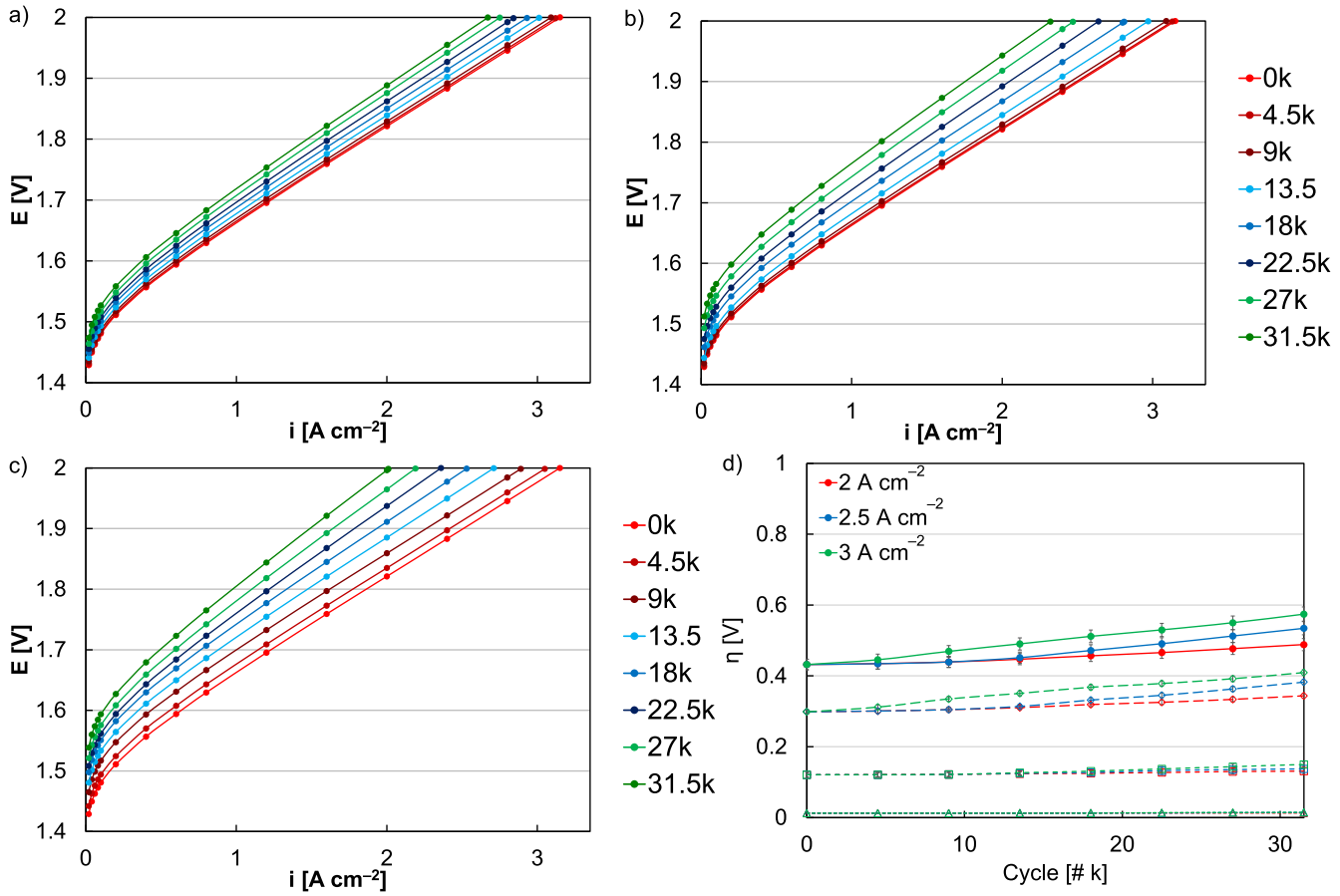

Figure 2. Changes to polarization curves as a function of durability testing for MEAs with an upper current density limit of (a) 2, (b) 2.5, and (c) 3 A cm^{-2}. (d) Changes to overpotential in durability testing for MEAs with an upper current density limit of 2 (red), 2.5 (blue), and 3 A cm^{-2} (green). Losses were included for the total overpotential (solid line, filled circles) and due to kinetics (long dashed line, open diamonds), ohmic (short dashed line, open squares), and transport (dotted line, open triangles). Durability testing was completed by square-wave current density cycles, 30 s at 2.5 A cm^{-2} followed by 30 s at 0 A cm^{-2} at 80 °C.

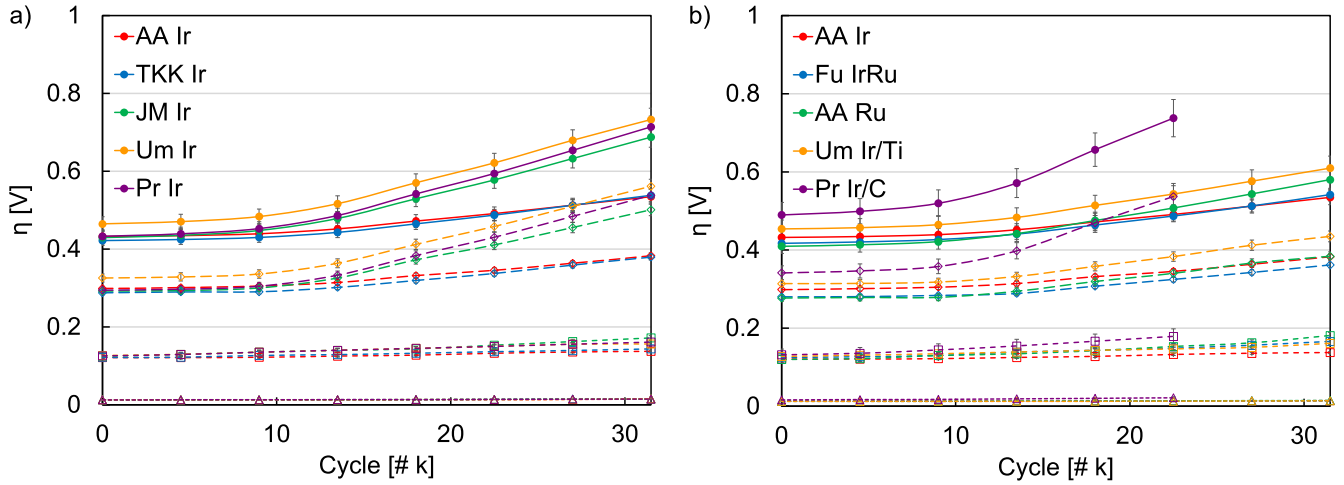

Figure 3. Changes to overpotential at 1 A cm^{-2} in durability testing for MEAs with different anode catalysts. Materials were separated into (a) Ir-only and (b) those containing Ru or supports. Losses were included for the total overpotential (solid line, filled circles) and due to kinetics (long dashed line, open diamonds), ohmic (short dashed line, open squares), and transport (dotted line, open triangles). Durability testing was completed by square-wave current density cycles, 30 s at 2.5 A cm^{-2} followed by 30 s at 0 A cm^{-2} at 80 °C.

catalyst layer to higher potential. Several aspects related to the titania support, including additional resistances and changes to catalyst layer integration, may have also affected the initial performance and loss rate in durability testing. Additionally, much larger losses were found with Pr Ir/C (11.0 μV cycle^{-1}) and durability testing was stopped at 22,500 cycles to prevent higher cell potentials and possible damage to the PTL coating. The high loss rate in this case was like due to the high metal content (Ir) and oxidation/delamination concerns with the carbon support.

Detailed performance and ex situ characterization data were presented for four of the evaluated catalysts for additional insight (Fig. 4). The catalysts included Alfa Aesar Ir, TKK Ir, Johnson

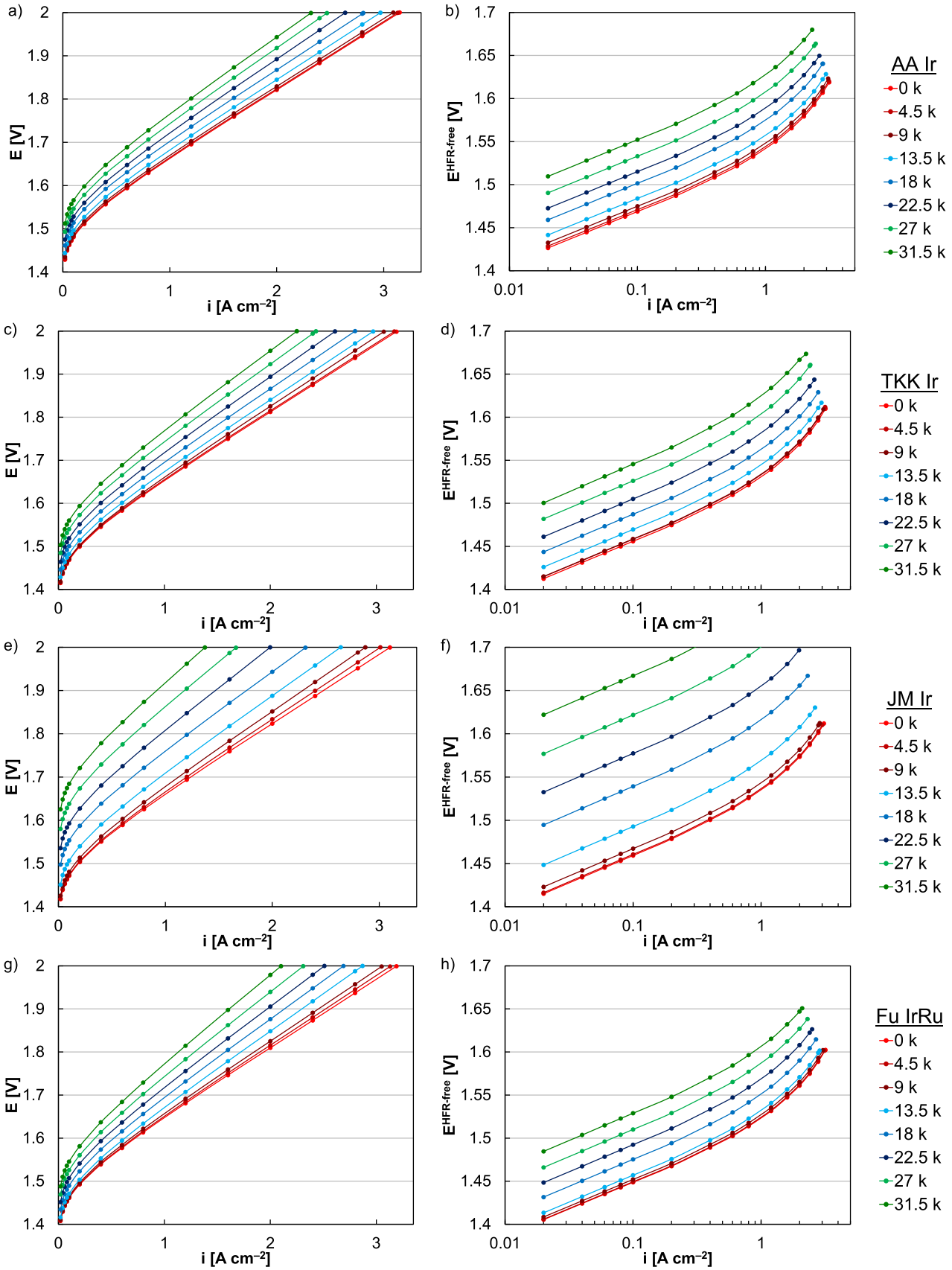

Figure 4. Changes to polarization curves and Tafel plots as a function of durability testing for MEAs with (a)–(b) Alfa Aesar Ir, (c)–(d) TKK Ir, (e)–(f) Johnson Matthey Ir, and (g)–(h) Furuya IrRu as the anode catalyst. Durability testing was completed by square-wave current density cycles, 30 s at 2.5 A cm^{-2} followed by 30 s at 0 A cm^{-2} at 80 °C.

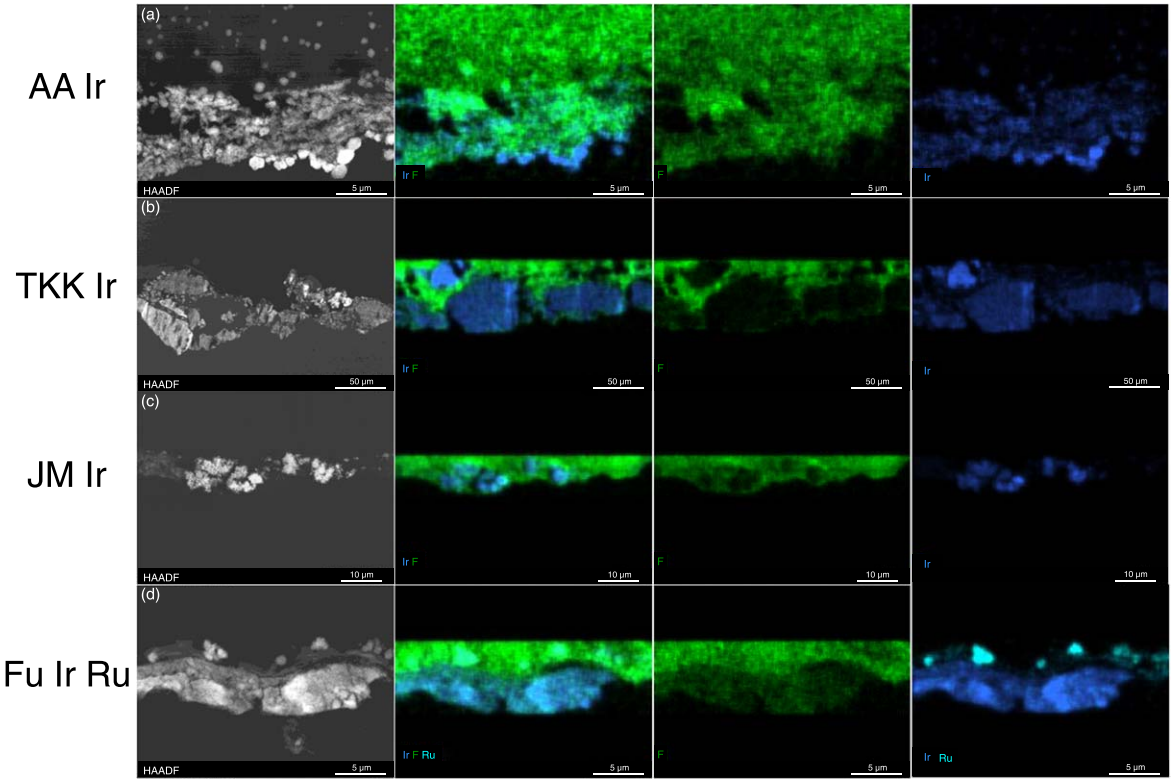

Figure 5. HAADF-STEM and EDS spectrum images (Ir, F) of cross-sectioned anode catalyst layers from MEAs with (a) Alfa Aesar Ir, (b) TKK Ir, (c) Johnson Matthey Ir, and (d) Furuya IrRu anode catalyst layers following accelerated stress tests. Durability testing was completed by square-wave current density cycles, 30 s at 2.5 A cm^{-2} followed by 30 s at 0 A cm^{-2} at 80 °C.

Matthey Ir, and Furuya IrRu and focused on MEAs that were more durable (Alfa Aesar Ir, TKK Ir, Furuya IrRu) and utilized catalysts with different properties (metal/oxide, Ir-only and Ru-containing). As with all catalysts evaluated, performance losses were generally due to declining kinetics, although smaller ohmic and transport loss occurred as well. Kinetic loss corresponded to large decreases in exchange current density, which dropped by orders of magnitude (Alfa Aesar Ir 30 times, Johnson Matthey 1400 times). While the kinetic performance clearly decreased, the Tafel slope or mechanism did not significantly change. Consistent trends were also observed with in situ diagnostics, where the capacitances decreased (cycling voltammograms) and the polarization resistance increased (impedance spectra). As with cell performance and loss type, diagnostic changes occurred in the same way and with similar proportions, and only the severity changed. In all cases, performance losses were relatively low at the start of the stress test, and increased to a higher rate after approximately 150 h. Slow loss rates initially may be due to competing degradation (catalyst dissolution/migration, layer changes) and conditioning (catalyst/ionomer reordering, hydration, contaminant removal) processes and longer conditioning times or more aggressive break-in conditions may improve initial performance and change the initially slow loss rate. Performance losses were also affected by potential and increasing cell potential may have increased degradation and loss rates toward the end of testing.

Following durability testing, MEAs were cross-sectioned and evaluated with microscopy and EDS to assess how degradation changed with different catalysts. For the Ir oxide baseline (Alfa Aesar), Ir migration into the membrane interface was found although significant amounts of the catalyst remained (Fig. 5). While performance changes were primarily kinetic and likely due to decreasing site-access, large-scale catalyst/ionomer segregation was not observed after testing. For the other catalysts, however, the ionomer did not appear to be uniformly distributed and sections of Ir/Ru aggregated into spaces with little to no fluorine signal. In several instances, denser patches (HAADF images) of catalyst were found that may indicate particle agglomeration. For TKK Ir and Furuya IrRu in particular, larger blocks of catalyst appeared to form that were not representative of their ex situ surface area. These differences may be due to the lower oxide content (Johnson Matthey Ir, TKK Ir, Furuya IrRu) increasing dissolution and material mobility, allowing for catalyst agglomeration and catalyst/ionomer segregation through dissolution and reprecipitation during load cycling. Additionally, the Johnson Matthey Ir catalyst layer was much thinner after durability testing and likely indicated higher degrees of catalyst dissolution and migration. For the Furuya IrRu catalyst, clear separation was also found where the Ru migrated into the membrane and Ir (primarily) remained in the catalyst layer.

Cross-sectioned MEAs were also evaluated with SEM to assess differences over slightly larger regions spatially (Fig. 6). In most cases, bare batches of catalyst or complete catalyst layer loss were not found. For Johnson Matthey Ir, however, instances were found with little to no catalyst at the membrane interface which were consistent with the high metal content, higher dissolution rate, and the larger MEA performance losses in durability testing. Additionally and as with TEM, bright or denser sectioned were also found in the TKK Ir and Furuya IrRu catalysts layers that may indicate some degree of particle agglomeration.

X-ray scattering characterization was performed on the anodes removed from the membrane of select MEAs from the set shown in Fig. 4. Particle volume distribution functions derived from fitting the X-ray scattering results (Fig. 7) show that the JM Ir catalyst had the largest volume fraction of particles >20 nm diameter, followed by AA IrO_x, TKK IrO_x, and Furuya IrO_x/RuO_x. This order of decreasing volume fraction of particles >20 nm in diameter agrees with the increasing post-cycling kinetic losses for these for catalysts shown in Fig. 3 indicating that catalyst particle size/surface area may be a factor influencing the observed kinetic loss trends. It should be noted, however, that X-ray scattering is not specific to the Ir particles and these measurements probe only catalyst particles remaining in the anode and not those deposited in the membrane.

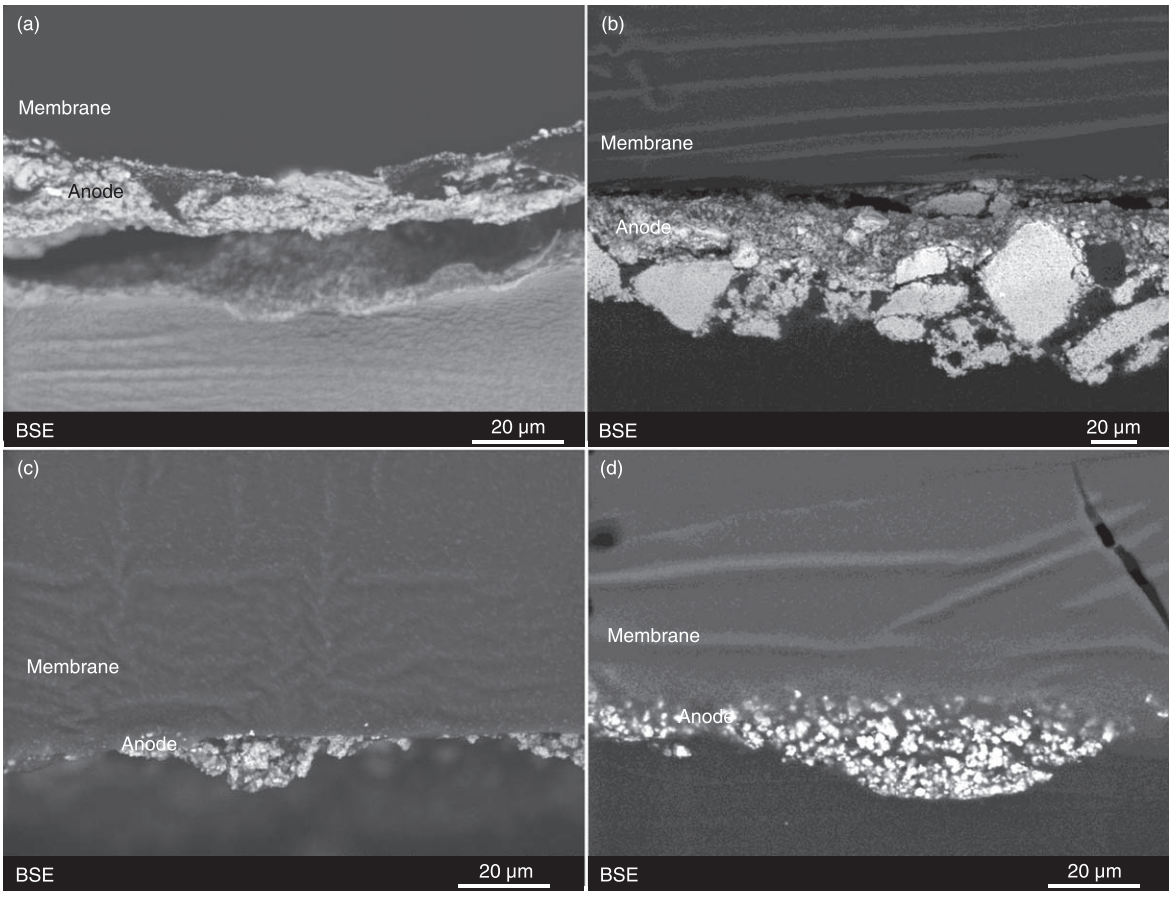

Figure 6. SEM images of cross-sectioned anode catalyst layers from MEAs with (a) Alfa Aesar Ir, (b) TKK Ir, (c) Johnson Matthey Ir, and (d) Furuya IrRu anode catalyst layers following accelerated stress tests. Durability testing was completed by square-wave current density cycles, 30 s at 2.5 A cm^{-2} followed by 30 s at 0 A cm^{-2} at 80 °C.

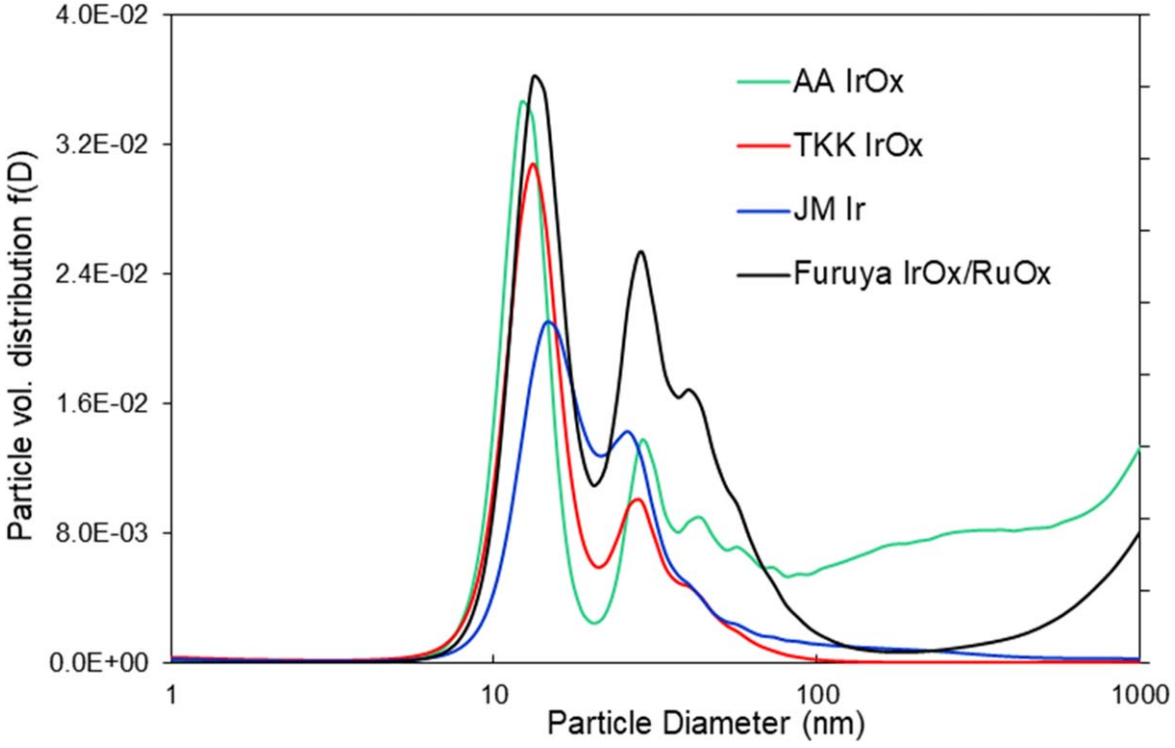

Figure 7. Anode catalyst particle volume distribution functions derived from small-angle X-ray scattering (SAXS) data for cycled MEAs. Durability testing was completed by square-wave current density cycles, 30 s at 2.5 A cm^{-2} followed by 30 s at 0 A cm^{-2} at 80 °C.

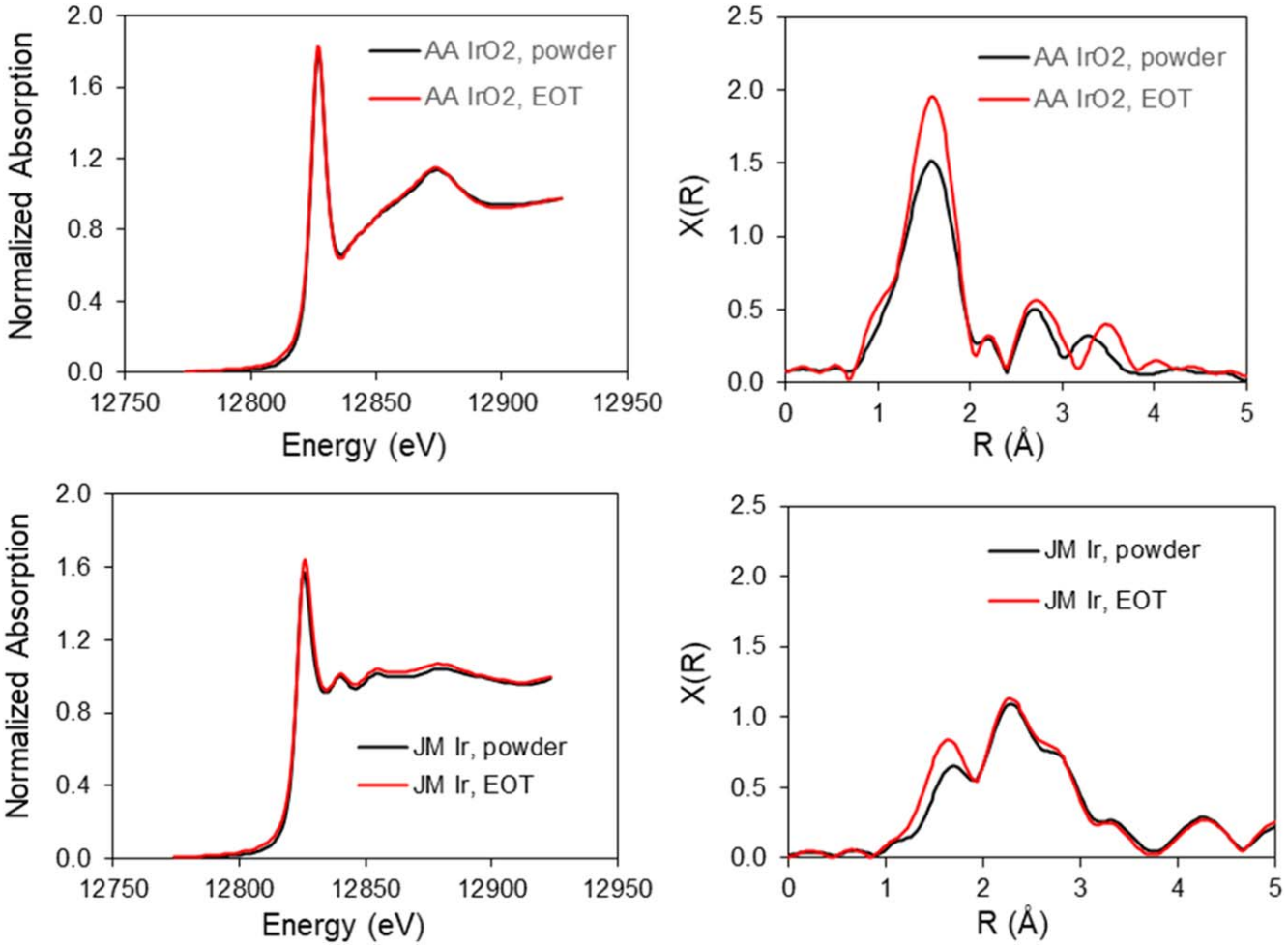

Figure 8. Ir L_2 XANES (left) and Fourier transforms of the Ir L_2 extended X-ray absorption fine structure (right) for catalyst powders and anodes from cycled MEAs. Durability testing was completed by square-wave current density cycles, 30 s at 2.5 A cm^{-2} followed by 30 s at 0 A cm^{-2} at 80 °C.

The extent of oxidation of Ir in cycled MEAs was determined using Ir L_2 edge X-ray absorption spectroscopy. The near-edge region of the spectra (XANES) and the Fourier transform of the extended region are shown in Fig. 8 for two of the post-cycling anodes and the corresponding catalyst powders, AA IrO_x and JM Ir. The height of the peak of the absorption in the XANES region, also termed the "white line," is indicative of the extent of oxidation of the Ir, as is the magnitude of the scattering peak at ∼1.5 Å in the Fourier transform, which can be attributed to Ir-O scattering. The peak at ∼2.3 Å in the Fourier transform arises from Ir-Ir scattering in Ir metal. Based on both the height of the white line and the magnitude of the scattering peak at ∼1.5 Å, incorporation into the MEA and cycling caused slight oxidation of the AA IrO_2 and the JM Ir. The EXAFS of the TKK and Furuya powders used to fabricate these MEAs were not measured.

The XANES regions of the Ir L_2 edge absorption data for the four anodes are compared in Fig. 9. These data show that after cycling the Ir in the AA IrO_x anode has the highest extent of oxidation, followed by the Furuya IrO_x/RuO_x, and TKK IrO_x, with JM Ir having the lowest extent of oxidation. These extents of oxidation can be quantified using linear combination fitting of the XANES regions of the anodes to the XANES regions for two standards: JM Ir powder and TKK IrO_2 powder, which were found by wide-angle X-ray scattering, X-ray diffraction, and analysis of the extended X-ray absorption data to be predominantly metallic and rutile IrO_2, respectively. The results of the linear combination fitting are shown in Table I. These results show that approximately 43 atomic percent of the Ir in the TKK IrO_x is present as metallic Ir after cycling in an MEA and 5 atomic percent of the JM Ir is oxidized as a result of cycling.

Further ex situ characterization was completed to compare dissolution rates, metal/oxide content, and to correlate materials properties to observed activities/performances. Ex situ evaluations of dissolution rates used holds (13.5 h) at a variety of potentials (1.4–2 V) in rotating disk electrode half-cells to focus on catalyst dissolution and avoid other mechanisms for catalyst layer degradation, including catalyst agglomeration, ionomer loss, and interfacial tearing. Rotating disk electrode testing incorporates transport limitations, and bubble formation can result in gas blinding or lower dissolution rates due to a lack of site-access during the experiment duration. Past efforts with a single catalyst (Alfa Aesar Ir), however, proved useful in understanding the impact of different load profiles on catalyst dissolution and MEA performance loss. For the evaluated materials, dissolution significantly increased with potential. While dissolution generally began at potentials higher than 1.4 V, Furuya IrRu and Alfa Aesar Ru both saw Ru dissolution at 1.4 V and was likely due to the lower thermodynamic potential for Ru as a dissolved species.

Catalysts were also evaluated in rotating disk electrode half-cells to determine their ECA, approximate metal/oxide content, and OER activity (Figs. 10a, 10b). ECA measurements and metal/oxide determinations rely on a combination of hydrogen underpotential deposition, capacitance, and mercury underpotential deposition measurements. These tests leverage past efforts developing ECA measurement protocols for Ir catalysts and adapting these protocols to Ru-containing materials.[40] Hydrogen underpotential deposition

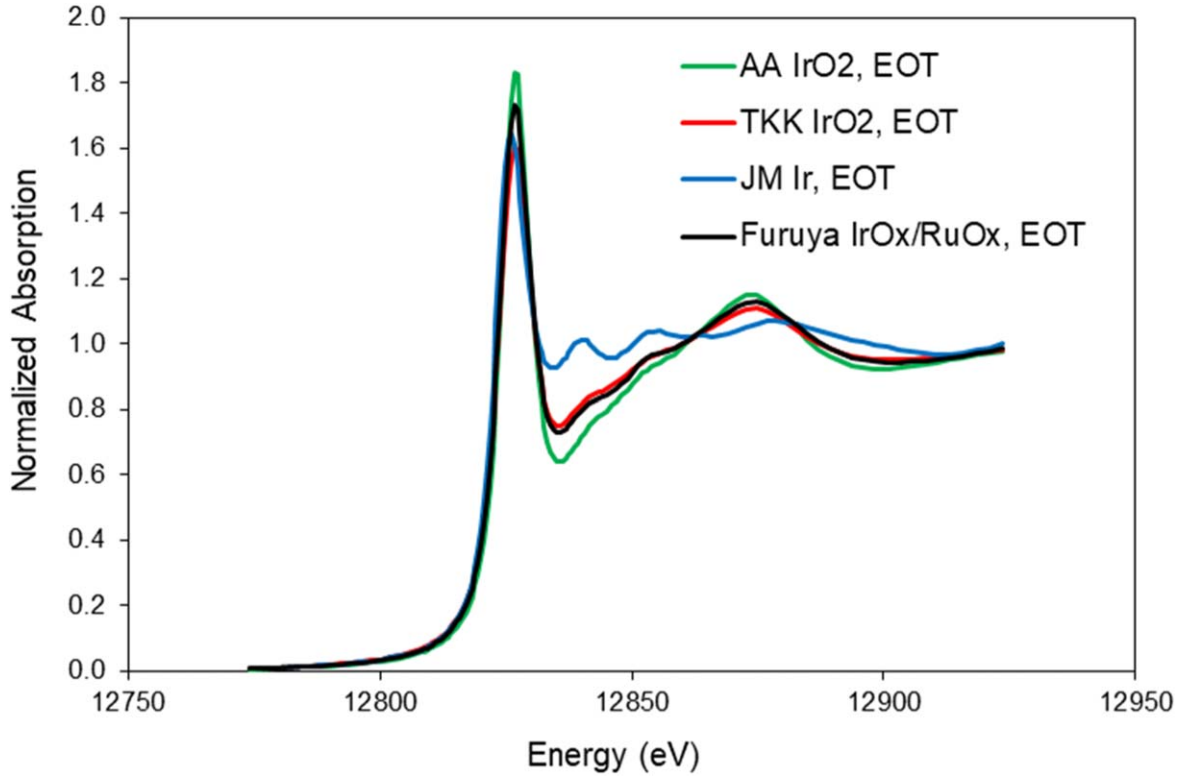

Figure 9. Ir L_2 XANES of the four select anodes after cycling in an MEA. Durability testing was completed by square-wave current density cycles, 30 s at 2.5 A cm^{-2} followed by 30 s at 0 A cm^{-2} at 80 °C.

Table I. Results of linear combination fitting of Ir L_2 XANES for cycled anodes to XANES for rutile IrO_2 (TKK IrO_2 powder) and metallic Ir (JM Ir powder). MEA exchange current densities, initial and end of test (EOT), were included for the catalysts. Durability testing was completed by square-wave current density cycles, 30 s at 2.5 A cm^{-2} followed by 30 s at 0 A cm^{-2} at 80 °C.

Sample	Mole fraction IrO_2	Mole fraction Ir metal	Exchange current density [A cm^{-2}]	EOT exchange current density [A cm^{-2}]
AA IrO_x, powder	0.94 ± 0.02	0.06 ± 0.02	—	—
AA IrO_x, EOT	1 ± 0.02	0 ± 0.02	6.6×10^{-7}	2.5×10^{-8}
JM Ir, powder	0	1	—	—
JM Ir, EOT	0.05 ± 0.02	0.95 ± 0.02	1.6×10^{-6}	1.1×10^{-9}
TKK IrO_x, EOT	0.57 ± 0.03	0.43 ± 0.03	1.4×10^{-6}	8.8×10^{-8}
Furuya IrO_x/RuO_x, EOT	0.67 ± 0.02	0.33 ± 0.02	1.8×10^{-6}	1.2×10^{-7}

was used to determine the metal ECA, since hydrogen adsorption will occur on metals but not oxides. Capacitance was used to qualitatively evaluate the oxide content. While capacitance is not surface sensitive, the capacitances of Ir/Ru oxides are larger, and the measurement is useful in qualitatively confirming a high oxide content. Mercury underpotential deposition was used to determine the total surface area available electrochemically and can adsorb/desorb onto metals and oxides, provided that electrodes are conditioned to low potential to substitute mercury for adsorbed oxygen.

When comparing the ECAs (metal/oxide evaluations), dissolution rates, and MEA durabilities, two overarching trends were observed. First and for the Ir-only catalysts, materials that were primarily metallic showed higher dissolution rates (Fig. 11) and higher activity/performance losses in rotating disk electrodes and MEAs. Examples include Johnson Matthey Ir, Umicore Ir, Premetek Ir, and Premetek Ir/C; the high metal content for these catalysts was confirmed in XRD (Figs. 10c, 10d) and electrochemically, where the metal ECA was similar to the total ECA, and the capacitance was qualitatively lower than the fully oxidized baseline (Alfa Aesar Ir). In MEAs, the performance loss rates for these catalysts were significantly higher (Johnson Matthey Ir 8.2 μV $cycle^{-1}$, Umicore Ir 8.5 μV $cycle^{-1}$, Premetek Ir 8.9 μV $cycle^{-1}$, Premetek 11.0 μV $cycle^{-1}$) than the baseline oxide (Alfa Aesar Ir 3.3 μV $cycle^{-1}$); activity losses in half-cell testing for these catalysts was also total and corresponded to large decreases in surface area (metal, total, and capacitance). For Premetek Ir/C, the corrosion susceptible support likely added to catalyst delamination and increased MEA performance losses relative to other Ir metal catalysts. For TKK Ir, a mixture of metal/oxide was indicated by a metal ECA that was smaller than the total (hydrogen underpotential deposition 13% of mercury) and a moderate capacitance. The dissolution rate, activity loss (RDE 66%), and MEA performance loss rate (3.7 μV $cycle^{-1}$) were between the metal and oxide Ir catalysts. For Umicore Ir/Ti, the Ir was primarily an oxide, indicated by XRD, high capacitance, and low participation in hydrogen underpotential deposition. Both the ex situ dissolution rate and activity loss were similar to the Ir oxide baseline (Alfa Aesar Ir). The higher MEA performance loss rate (4.9 μV $cycle^{-1}$), however, was likely due to the lower initial performance and higher cell/anode potential during the stress test.

Second, Ru inclusion increased activity/performance losses compared to Ir oxide, but less so than Ir metal. For Alfa Aesar Ru, the high oxide content was confirmed with XRD and

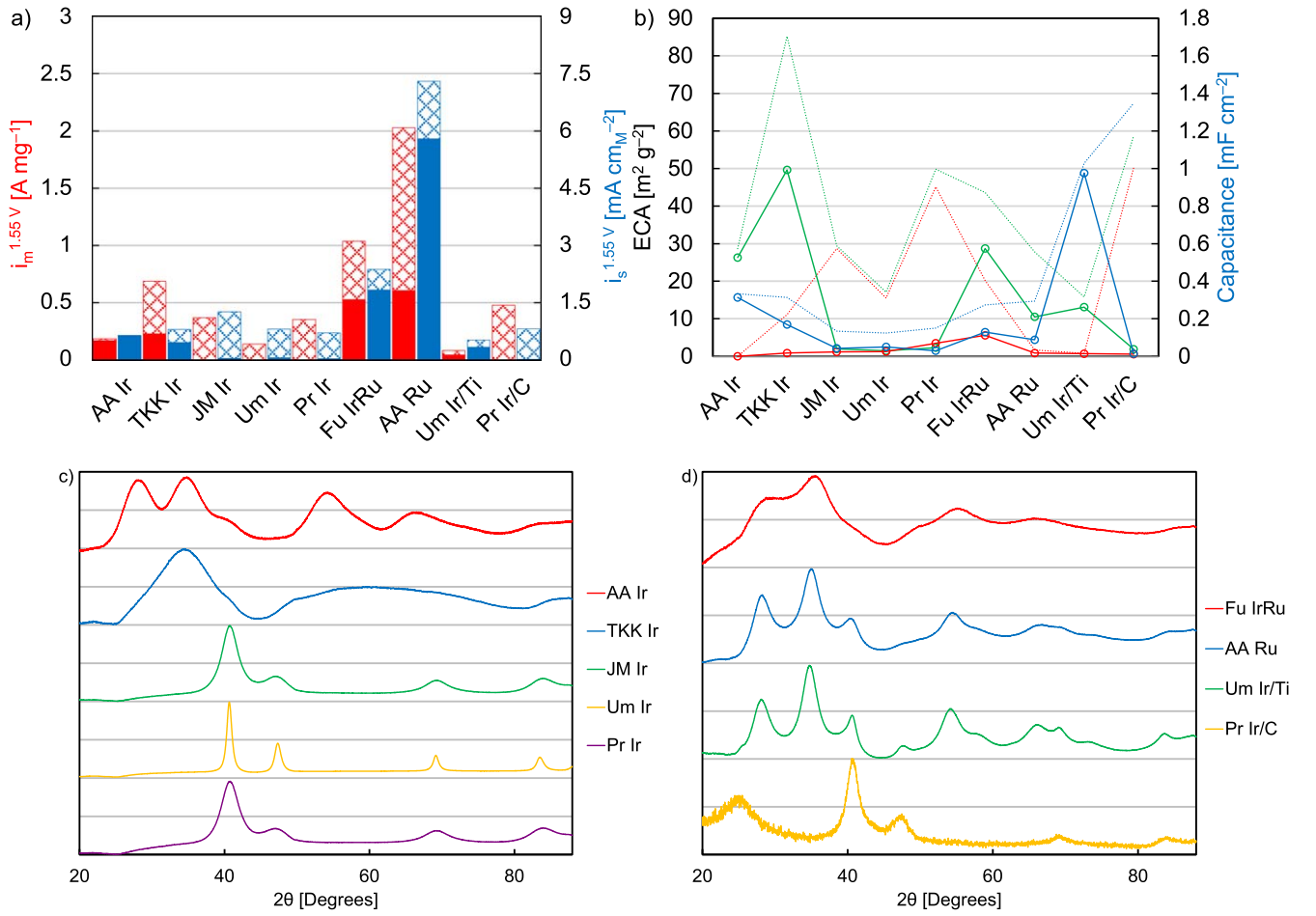

Figure 10. (a) Mass (red) and site-specific (blue) activities of screened catalysts in rotating disk electrode half-cells, prior to (shaded) and following (solid) durability testing (13.5 h, 2 V hold). Site-specific activities were calculated with ECAs determined by mercury underpotential deposition. (b) ECAs by hydrogen underpotential deposition (red), capacitances (blue), and ECAs by mercury underpotential deposition (green) of screened catalysts in rotating disk electrode half-cells, prior to (dotted line) and following (solid line) durability testing (13.5 h, 2 V hold). XRD patterns of (c) Ir-only and (d) supported and Ru-containing catalysts.

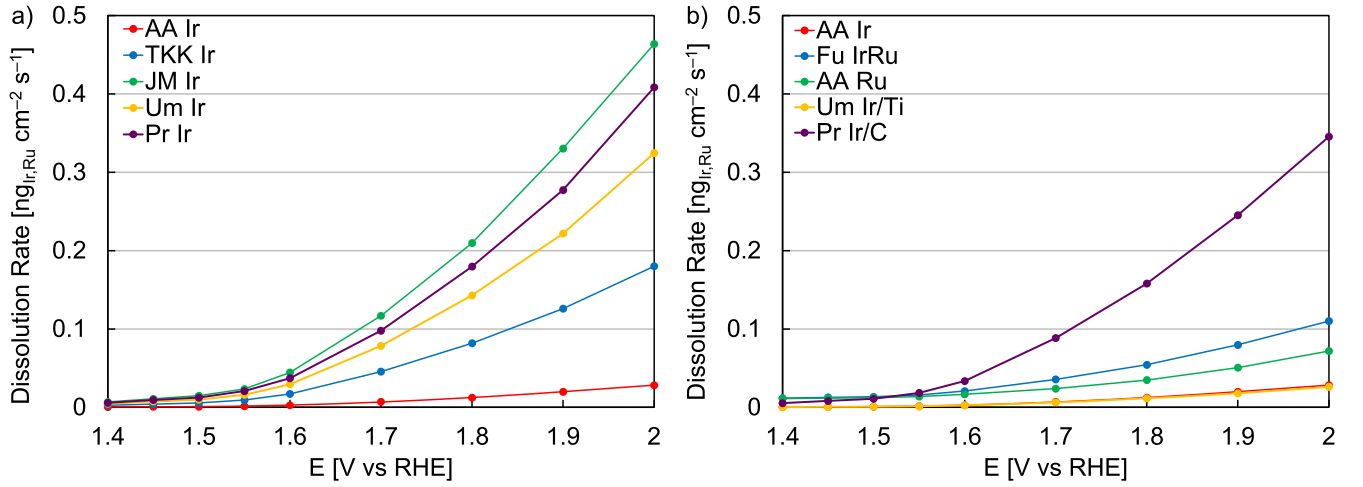

Figure 11. Dissolution rates at different potentials (1.4–2 V) in rotating disk electrode testing, for (a) Ir-only catalysts and (d) those containing Ru or supports. For all experiments, aliquots were taken for ICP-MS at 0.5, 1, 4, and 13.5 h.

electrochemically with the high capacitance and lack of participation in hydrogen underpotential deposition. As a Ru-only catalyst, the rotating disk electrode activity (70%) and MEA bperformance (5.4 μV cycle^{-1}) losses were higher than the Ir oxide baseline (Alfa Aesar Ir) but less than the Ir metal catalysts (total RDE, >8 μV cycle^{-1} MEA). Furuya IrRu contained a combination of metal/oxide at the surface, indicated by a metal ECA that was smaller than the total (hydrogen underpotential deposition 46% of

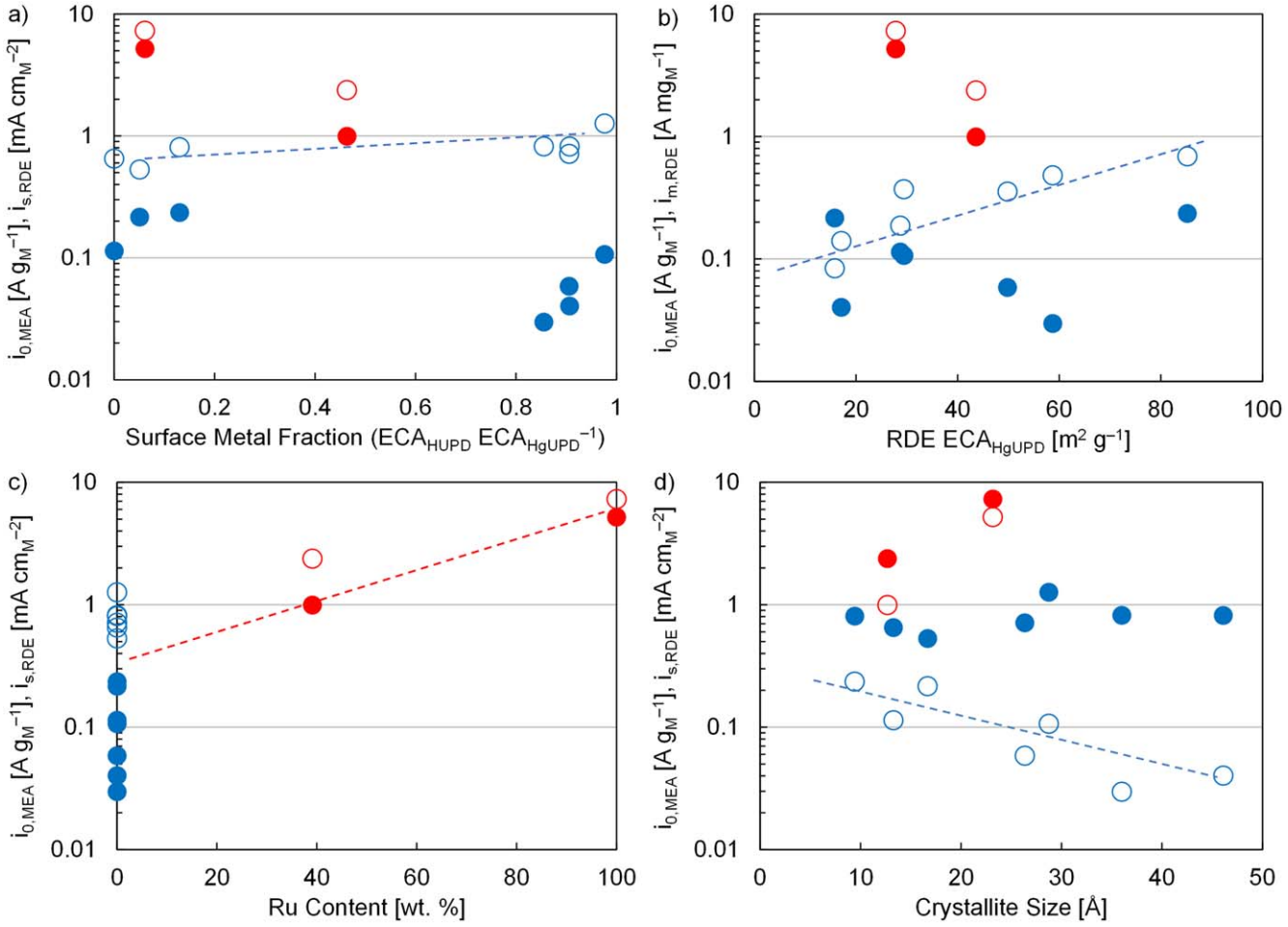

Figure 12. MEA exchange current densities at 80 °C for Ru containing (red solid circles) and Ir-only (blue solid circles) catalysts and rotating disk electrode activities at room temperature for Ru containing (red open circles) and Ir-only (blue open circles) catalysts as a function of (a) metal content in ECA measurements, (b) ECA by mercury underpotential deposition, (c) Ru content, and (d) crystallite size. Rotating disk electrode activities were determined at 1.55 V vs RHE and site-specific activities were calculated with ECAs determined by mercury underpotential deposition. Dashed lines denoted correlations discussed in the text.

mercury) and a moderate capacitance. During ex situ potential holds, the Ru dissolution rate was less than the Ir and likely due to the higher Ir composition. Compared to TKK Ir (also mixed metal/oxide content), the total dissolution rate for Furuya IrRu was similar but slightly lower; the rotating disk electrode activity loss (51%) and MEA performance loss rate (4.0 μV cycle^{-1}) were also similar.

Materials properties were evaluated for their impact on performance and durability in rotating disk electrodes and MEAs. While most characteristics had a partial or loose effect, Ru inclusion clearly improved kinetics in rotating disk electrodes (specific activity) and MEAs (exchange current density, Fig. 12c). In both ex and in situ testing, the Ru-containing catalysts outperformed those that were Ir-only; high Ru content (Alfa Aesar Ru) further improved activity/performance beyond the Ir/Ru mixed catalyst. Furthermore, Ru inclusion appeared to be the largest factor examined and had to be separated (red circles) from the Ir-only catalysts (blue circles) when evaluating other properties. For metal/oxide composition, higher metal content within Ir-only catalysts improved ex situ activity, and the activity of Ir metal was double that of Ir oxide (Fig. 12a). Higher metal activity, however, did not translate to MEA testing. This mismatch in activity/performance was related to near-surface oxide content and differences in conditioning protocols in the two approaches. In rotating disk electrodes, electrochemical conditioning was completed over roughly 10 min at room temperature (50 cycles, 1.2–1.8 V vs RHE, 100 mV s^{-1}) and can preserve subsurface metal or mixed oxide content. MEAs, however, were conditioned at a higher temperature (80 °C) over a longer period of time. The higher time and temperature likely increased the oxide content near-surface in catalysts that were less than a full oxide ex situ, lessening lattice strain and strengthening Ir-O binding, and lowering oxygen evolution activity.[51] Similarly, higher ECA improved Ir-only mass activity (rotating disk electrode) but did not appear to dramatically affect MEA performance (Fig. 12b). Thin catalyst layers in rotating disk electrodes can allow for a high degree of site utilization and higher ECA can significantly improve activity. For these materials at the device-level, however, most were unsupported, did not vary greatly in ex situ particle size (<5 nm), and tended to form thin, less porous catalyst layers which may lessen the impact of ECA within limited material sets. Finally, crystallite size appeared to affect ex situ Ir-only activity, with more amorphous materials demonstrating higher OER activity (Fig. 12d). This correlation, however, did not appear to translate to MEAs, where longer conditioning times may amorphize surfaces and negate the impact of ex situ crystallinity.[51,53]

When comparing trends in materials properties to durability, a wide range of ex situ dissolution rates and in situ performance losses were found. Qualitatively, there was a reasonable correlation between dissolution in rotating disk electrodes and MEA performance losses, and catalysts that were more prone to dissolve at high potential tended to make for less durable MEAs. For metal/oxide composition, higher metal content generally increased both

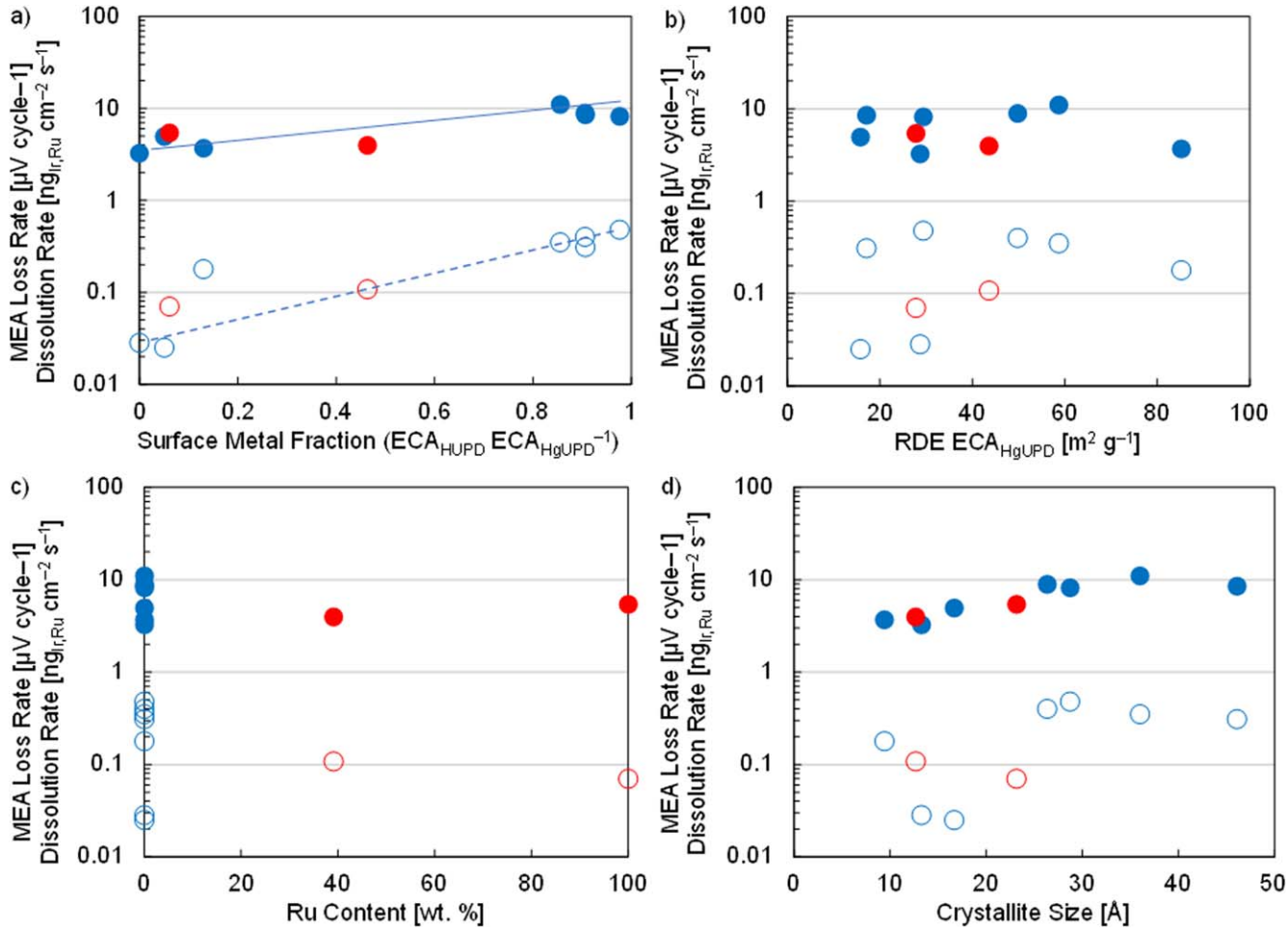

Figure 13. MEA loss rates for Ru containing (red solid circles) and Ir-only (blue solid circles) catalysts and rotating disk electrode dissolution rates at room temperature for Ru containing (red open circles) and Ir-only (blue open circles) catalysts as a function of (a) metal content in ECA measurements, (b) ECA by mercury underpotential deposition, (c) Ru content, and (d) crystallite size. Rotating disk electrode dissolution rates were determined at 2 V through aliquots analyzed by ICP-MS during a 13.5 h hold at room temperature (Fig. 11). MEA loss rates were calculated from overpotential changes at 1 A cm^{-2} during durability testing by square-wave current density cycles, 30 s at 2.5 A cm^{-2} followed by 30 s at 0 A cm^{-2} at 80 °C.

dissolution and MEA loss rates (Fig. 13a). This result was expected due to the increased dissolution kinetics of Ir and Ru metals compared to oxides, and since higher dissolution rates appeared to increase the mobility and migration of catalyst layers in MEA testing (Fig. 5). The relationship between other materials properties (ECA, Ru content, crystallite size) and dissolution/degradation, however, was less clear. This was likely due to the metal content dominating dissolution and MEA loss rates compared to other properties, and controlled systems varying single parameters would be more valuable in definitively correlating materials properties to degradation. Dissolution in rotating disk electrodes may also be useful for an initial screening, but loses some of the complexity of device-level durability testing, including the impact of initial performance on load requirements and catalyst layer changes or interfacial degradation that may be more driven by current than catalyst dissolution.

The rotating disk electrode dissolution rates (Fig. 11) and MEA loss rates were analytically fit to the exposed potential (1.4–2 V, for rotating disk electrode dissolution rates) and catalyst properties, including the metal content (0–98%), ECA by mercury underpotential deposition (15.8–85.2 $m^2\ g^{-1}$), Ru content (0–100%), and crystallite size (9.4–46.1 Å). For rotating disk electrode dissolution rates, fitting began with the most critical parameter (voltage). For dissolution and MEA loss rates, fitting followed with adjustment factors by impact, in the order of metal content, ECA, Ru content, and crystallite size. For rotating disk electrode dissolution rates, fitting yielded the equation:

$$D = (0.7051V^2 - 2.0049V + 1.4282) \times (0.1863e^{2.3629M}) \times (0.0006ECA^2 - 0.0353ECA + 1.271) \times (0.0002Ru^2 - 0.0072Ru + 0.9749) \times (0.8719e^{0.0033C})$$

where D is the rotating disk electrode dissolution rate in $ng_{Ir,Ru}$ $cm^{-2}\ s^{-1}$, V is the applied potential in volts, M is the metal content in fraction (0–1), ECA is the ECA by mercury underpotential deposition in $m^2\ g^{-1}$, Ru is the Ru content in fraction (0–1), and C is the crystallite size in Å. For the materials evaluated in this study, the above analytical equation fit the presented data (81 dissolution rate data points) with a R^2 value of 0.93 by the equation:

$$R^2 = 1 - \frac{\sum(y_i - \hat{y}_i)^2}{\sum(y_i - \bar{y})^2}$$

For MEA loss rates, fitting yielded the equation:

$$MEA = (3.843e^{0.8885M}) \times (0.000004ECA^2 - 0.0022ECA + 1.1047) \times (0.0002Ru^2 - 0.0157Ru + 1.005) \times (0.8883e^{0.0038C})$$

where MEA is the MEA loss rate in $\mu V\ cycle^{-1}$, M is the metal content in fraction (0–1), ECA is the ECA by mercury underpotential deposition in $m^2\ g^{-1}$, Ru is the Ru content in fraction (0–1), and C is the crystallite size in Å. For the materials evaluated in this

study, the above analytical equation fits the presented data (9 averaged loss rates) with a R^2 value of 0.81.

This type of fitting is limited in that the materials studied are a small set of commercial catalysts that vary multiple properties simultaneously. Individual parameters such as the metal content may have dictated much of the dissolution and loss rates, both due to the comparatively large range of materials explored and its relatively influence on stability and durability. Controlled systems varying single parameters would be more valuable in definitively correlating materials properties to a dissolution rate. These analytical fits, however, were provided to establish quantitative relationships for the material set evaluated.

These results, both the correlations between ex and in situ performance and catalyst screenings with MEA stress tests, have implications related to the primary thrusts of catalyst development in proton exchange membrane electrolysis. Efforts historically have focused on Ru inclusion and the use of metals or less oxidized surfaces to improve activity and minimize durability losses through lower load requirements. While Ru inclusion clearly improves OER activity, these performance advantages were lost during stress tests after a relatively short period of time. These results were also consistent with past efforts focused on less aggressive stressors (moderate loading, constant input). For other materials properties, whether metal/oxide content or crystallinity, many of these enhancements do not appear to translate to in situ testing or provide a benefit in MEA performance or durability. In this way, a shift from purely materials discovery toward integration (supports, morphologies, structures) may be more effective in the future at device-level enhancements.[9] Although numerous catalyst development efforts have focused on approaches that can alter catalyst layer properties and performance/durability in the device, the purpose of this study was to evaluate commercially available materials.

Conclusions

This study evaluated options for accelerated stress tests in low temperature electrolysis that focus on anode catalyst layer degradation due to intermittent operation. To increase performance loss and shorten experiment duration, testing used low catalyst loading and frequent load cycling. Anode catalysts screenings utilized square-wave cycles 0–2.5 A cm^{-2} to ensure a moderate performance loss without creating higher cell potentials that may incorporate additional loss mechanisms.

Several catalysts were screened, and included Ir-only, supported, and Ru-containing materials. Ru inclusion improved initial MEA performance and at 1 A cm^{-2}, overpotentials were lower than the Ir oxide baseline (by 15 mV Furuya IrRu, 23 mV Alfa Aesar Ru) and the highest performing Ir-only catalyst (by 5 mV Furuya IrRu, 12 mV Alfa Aesar Ru). These performance advantages, however, were lost following frequent load cycling and the overpotentials became higher than the Ir oxide baseline (by 7 mV Furuya IrRu, 45 mV Alfa Aesar Ru). With Ir catalysts that were not fully oxidized, higher ex situ activity did not translate to higher in situ performance. Higher losses, however, were found and ranged from 3.7 μV $cycle^{-1}$ for majority oxide (87% surface, TKK Ir) to 8–9 μV $cycle^{-1}$ for primarily metallic catalysts. These durability differences were likely due to the increased dissolution rate of Ir metal and corresponded to thinner catalyst layers and bare patches after testing. While other factors, including surface area and crystallinity, appeared to have an impact in ex situ activity, a minimal effect on device-level performance and durability was found.

These results establish an option for accelerated stress tests that focus on anode catalyst layer durability due to intermittent operation. Catalyst screenings were consistent with historical findings in literature (increased loss rates with ruthenium and substoichiometric oxide inclusion) and rationalize the continued use of iridium oxide as a baseline catalyst. As traditional catalyst development approaches did not dramatically improve device-level durability, a shift in focus toward integration (supports, morphologies, structures) may be more effective at minimizing performance losses, and efforts in this area are critical to improving in situ catalyst utilization and lessening load requirements. Additionally, the inclusion of other catalyst and component loss mechanisms is critical to understanding electrolyzer degradation, developing device-level accelerated stress tests, and managing electrolyzer cost and lifetime under future anticipated operating conditions.

Acknowledgments

This work was authored by the National Renewable Energy Laboratory, operated by Alliance for Sustainable Energy, LLC, for the U.S. Department of Energy (DOE) under Contract No. DE-AC36–08GO28308. The submitted manuscript has been created in part by UChicago Argonne, LLC, Operator of Argonne National Laboratory ("Argonne"). Argonne, a U.S. Department of Energy Office of Science laboratory, is operated under Contract No. DEAC02–06CH11357. Funding was provided by U.S. Department of Energy Office of Energy Efficiency and Renewable Energy, Hydrogen and Fuel Cell Technologies Office through H2@Scale and the H2NEW Consortium. Electron microscopy was conducted at the Center for Nanophase Materials Sciences, which is a DOE Office of Science User Facility. The X-ray absorption (MRCAT, 10-BM and 10-ID) and scattering (XSD, 9-ID-C) experiments were performed at the Advanced Photon Source (APS), a DOE Office of Science User Facility operated for the DOE Office of Science by Argonne under Contract No. DE-AC02–06CH11357. The operation of MRCAT at the APS is supported by the Department of Energy and the MRCAT member institutions. The authors would like to thank Jan Ilavsky and Ivan Kuzmenko of the APS 9-ID-C.

The views expressed in the article do not necessarily represent the views of the DOE or the U.S. Government. The U.S. Government retains and the publisher, by accepting the article for publication, acknowledges that the U.S. Government retains a nonexclusive, paid-up, irrevocable, worldwide license to publish or reproduce the published form of this work, or allow others to do so, for U.S. Government purposes.

ORCID

Shaun M. Alia https://orcid.org/0000-0002-7647-9383
Nancy N. Kariuki https://orcid.org/0000-0002-6123-7373
Deborah J. Myers https://orcid.org/0000-0001-9299-3916
David A. Cullen https://orcid.org/0000-0002-2593-7866

References

1. IRENA, *Green Hydrogen Cost Reduction: Scaling up Electrolysers to Meet the 1.5 °C Climate Goal* (International Renewable Energy Agency, Abu Dhabi) (2020).
2. B. Pivovar, N. Rustagi, and S. Satyapal, *The Electrochemical Society Interface*, **27**, 47 (2018).
3. K. Ayers, *Current Opinion in Electrochemistry*, **18**, 9 (2019).
4. K. Ayers, N. Danilovic, R. Ouimet, M. Carmo, B. Pivovar, and M. Bornstein, *Annual Review of Chemical and Biomolecular Engineering*, **10**, 219 (2019).
5. P. Denholm, R. Margolis, and J. Milford, *Production cost modeling for high levels of photovoltaics penetration* (National Renewable Energy Lab.(NREL), Golden, CO (United States)) (2008).
6. S. M. Alia, *H2@Scale: Experimental Characterization of Durability of Advanced ElectrolyzerConcepts in Dynamic Loading* (2019), https://hydrogen.energy.gov/pdfs/review19/ta022_alia_2019_o.pdf.
7. H. Xu, *High-Performance, Long-Lifetime Catalysts for Proton Exchange Membrane Electrolysis* (2017), https://hydrogen.energy.gov/pdfs/review17/pd103_xu_2017_o.pdf.
8. K. Ayers and C. Capuano, *High Efficiency PEM Water Electrolysis Enabled by Advanced Catalysts, Membranes and Processes* (2018), https://hydrogen.energy.gov/pdfs/review18/pd155_ayers_2018_p.pdf.
9. S. M. Alia, *Current Opinion in Chemical Engineering*, **33**, 100703 (2021).
10. K. Ayers, *High Efficiency PEM Water Electrolysis Enabled by Advanced Catalysts, Membranes and Processes* (2019), https://hydrogen.energy.gov/pdfs/review19/p155_ayers_2019_o.pdf.
11. K. A. Lewinski, D. van der Vliet, and S. M. Luopa, *ECS Trans.*, **69**, 893 (2015).
12. S. Siracusano, N. Van Dijk, R. Backhouse, L. Merlo, V. Baglio, and A. S. Aricò, *Renewable Energy*, **123**, 52 (2018).
13. K. E. Ayers, E. B. Anderson, C. Capuano, B. Carter, L. Dalton, G. Hanlon, J. Manco, and M. Niedzwiecki, *ECS Trans.*, **33**, 3 (2019).
14. C. Rakousky, U. Reimer, K. Wippermann, M. Carmo, W. Lueke, and D. Stolten, *J. Power Sources*, **326**, 120 (2016).

15. P. Lettenmeier, R. Wang, R. Abouatallah, B. Saruhan, O. Freitag, P. Gazdzicki, T. Morawietz, R. Hiesgen, A. S. Gago, and K. A. Friedrich, *Sci. Rep.*, **7**, 44035 (2017).
16. U. Babic, M. Tarik, T. J. Schmidt, and L. Gubler, *J. Power Sources*, **451**, 227778 (2020).
17. S. A. Grigoriev, K. A. Dzhus, D. G. Bessarabov, and P. Millet, *Int. J. Hydrogen Energy*, **39**, 20440 (2014).
18. S. M. Alia, S. Stariha, and R. L. Borup, *J. Electrochem. Soc.*, **166**, F1164 (2019).
19. H. Xu, *High-Performance, Long-Lifetime Catalysts for Proton Exchange Membrane Electrolysis* (2015), http://hydrogen.energy.gov/pdfs/review15/pd103_xu_2015_o.pdf.
20. A. Weiß, A. Siebel, M. Bernt, T.-H. Shen, V. Tileli, and H. Gasteiger, *J. Electrochem. Soc.*, **166**, F487 (2019).
21. K. E. Ayers, E. B. Anderson, C. Capuano, B. Carter, L. Dalton, G. Hanlon, J. Manco, and M. Niedzwiecki, *ECS Trans.*, **33**, 3 (2010).
22. D. Bessarabov, A. Kruger, S. M. Luopa, J. Park, A. A. Molnar, and K. A. Lewinski, *ECS Trans.*, **75**, 1165 (2016).
23. M. Hamdan, *Electrochemical Compression* (2017), https://hydrogen.energy.gov/pdfs/review17/pd136_hamdan_2017_o.pdf.
24. S. M. Alia, K. S. Reeves, J. S. Baxter, and D. A. Cullen, *J. Electrochem. Soc.*, **167**, 144512 (2020).
25. C. Rakousky, G. P. Keeley, K. Wippermann, M. Carmo, and D. Stolten, *Electrochim. Acta*, **278**, 324 (2018).
26. C. Liu et al., *Adv. Energy Mater.*, **11**, 2002926 (2021).
27. T. Schuler, T. J. Schmidt, and F. N. Büchi, *J. Electrochem. Soc.*, **166**, F555 (2019).
28. C. Liu, M. Carmo, G. Bender, A. Everwand, T. Lickert, J. L. Young, T. Smolinka, D. Stolten, and W. Lehnert, *Electrochem. Commun.*, **97**, 96 (2018).
29. P. Satjaritanun, M. O'Brien, D. Kulkarni, S. Shimpalee, C. Capuano, K. E. Ayers, N. Danilovic, D. Y. Parkinson, and I. V. Zenyuk, *iScience*, **23**, 101783 (2020).
30. M. Zlobinski, T. Schuler, F. N. Büchi, T. J. Schmidt, and P. Boillat, *J. Electrochem. Soc.*, **168**, 014505 (2021).
31. M. Bühler, F. Hegge, P. Holzapfel, M. Bierling, M. Suermann, S. Vierrath, and S. Thiele, *J. Mater. Chem. A*, **7**, 26984 (2019).
32. T. Lickert, M. L. Kiermaier, K. Bromberger, J. Ghinaiya, S. Metz, A. Fallisch, and T. Smolinka, *Int. J. Hydrogen Energy*, **45**, 6047 (2020).
33. M. Chandesris, V. Médeau, N. Guillet, S. Chelghoum, D. Thoby, and F. Fouda-Onana, *Int. J. Hydrogen Energy*, **40**, 1353 (2015).
34. P. Trinke, P. Haug, J. Brauns, B. Bensmann, R. Hanke-Rauschenbach, and T. Turek, *J. Electrochem. Soc.*, **165**, F502 (2018).
35. H. Xu, *High-Performance, Long-Lifetime Catalysts for Proton Exchange Membrane Electrolysis* (2016), https://hydrogen.energy.gov/pdfs/review16/pd103_xu_2016_o.pdf.
36. S. Khandavalli, J. H. Park, N. N. Kariuki, S. F. Zaccarine, S. Pylypenko, D. J. Myers, M. Ulsh, and S. A. Mauger, *ACS Appl. Mater. Interfaces*, **11**, 45068 (2019).
37. G. Bender, M. Carmo, T. Smolinka, A. Gago, N. Danilovic, M. Mueller, F. Ganci, A. Fallisch, P. Lettenmeier, and K. A. Friedrich, *Int. J. Hydrogen Energy*, **44**, 18 (2019).
38. E. Padgett, G. Bender, A. Haug, K. Lewinski, F. Sun, H. Yu, D. A. Cullen, A. J. Steinbach, and S. M. Alia, *J. Electrochem. Soc.*, **170**, 084512 (2023).
39. S. M. Alia and G. C. Anderson, *J. Electrochem. Soc.*, **166**, F282 (2019).
40. S. M. Alia, K. E. Hurst, S. S. Kocha, and B. S. Pivovar, *J. Electrochem. Soc.*, **163**, F3051 (2016).
41. S. P. Kounaves and J. Buffle, *J. Electrochem. Soc.*, **133**, 2495 (1986).
42. I. C. Man, H.-Y. Su, F. Calle-Vallejo, H. A. Hansen, J. I. Martínez, N. G. Inoglu, J. Kitchin, T. F. Jaramillo, J. K. Nørskov, and J. Rossmeisl, *Chem. Cat. Chem*, **3**, 1159 (2011).
43. S. M. Alia, K. S. Reeves, H. Yu, J. Park, N. Kariuki, A. J. Kropf, D. J. Myers, and D. A. Cullen, *J. Electrochem. Soc.*, **169**, 054517 (2022).
44. S. M. Alia, B. Rasimick, C. Ngo, K. Neyerlin, S. S. Kocha, S. Pylypenko, H. Xu, and B. S. Pivovar, *J. Electrochem. Soc.*, **163**, F3105 (2016).
45. S. M. Alia and N. Danilovic, *Frontiers in Energy Research*, **10**, 857663 (2022).
46. J. Ilavsky, P. R. Jemian, A. J. Allen, F. Zhang, L. E. Levine, and G. G. Long, *J. Appl. Crystallogr.*, **42**, 469 (2009).
47. J. Ilavsky, *J. Appl. Crystallogr.*, **45**, 324 (2012).
48. J. Ilavsky and P. R. Jemian, *J. Appl. Crystallogr.*, **42**, 347 (2009).
49. P. R. Jemian, J. R. Weertman, G. G. Long, and R. D. Spal, *Acta Metall. Mater.*, **39**, 2477 (1991).
50. B. Ravel and M. Newville, *J. Synchrotron Radiat.*, **12**, 537 (2005).
51. S. M. Alia, M.-A. Ha, G. C. Anderson, C. Ngo, S. Pylypenko, and R. E. Larsen, *J. Electrochem. Soc.*, **166**, F1243 (2019).
52. S. Cherevko, S. Geiger, O. Kasian, A. Mingers, and K. J. J. Mayrhofer, *J. Electroanal. Chem.*, **773**, 69 (2016).
53. M.-A. Ha and R. E. Larsen, *J. Electrochem. Soc.*, **168**, 024506 (2021).